Dual constraints with ALMA: new [O III] 88micron and dust-continuum observations reveal the ISM conditions of luminous LBGs at z ~ 7

Witstok, J.; Smit, R.; Maiolino, R.; Kumari, N.; Aravena, M.; Boogaard, L.; ... ; Schouws, S.T.M.

Citation

Witstok, J., Smit, R., Maiolino, R., Kumari, N., Aravena, M., Boogaard, L., ... Schouws, S. T. M. (2022). Dual constraints with ALMA: new [O III] 88micron and dust-continuum observations reveal the ISM conditions of luminous LBGs at z ~ 7. *Monthly Notices Of The Royal Astronomical Society*, *515*(2), 1751-1773. doi:10.1093/mnras/stac1905

MNRAS **000**, 1–23 (2022) Preprint 6 July 2022 Compiled using MNRAS LATEX style file v3.0

Dual constraints with ALMA: new [O III] 88 μm and dust-continuum observations reveal the ISM conditions of luminous LBGs at $z \sim 7$

Joris Witstok[1,2]★, Renske Smit[1,2,3]†, Roberto Maiolino[1,2,4], Nimisha Kumari[5], Manuel Aravena[6], Leindert Boogaard[7], Rychard Bouwens[9], Stefano Carniani[8], Jacqueline A. Hodge[9], Gareth C. Jones[1,2,10], Mauro Stefanon[9], Paul van der Werf[9], and Sander Schouws[9]
[1] *Kavli Institute for Cosmology, University of Cambridge, Madingley Road, Cambridge CB3 0HA, UK*
[2] *Cavendish Laboratory, University of Cambridge, 19 JJ Thomson Avenue, Cambridge CB3 0HE, UK*
[3] *Astrophysics Research Institute, Liverpool John Moores University, 146 Brownlow Hill, Liverpool L3 5RF, UK*
[4] *Department of Physics and Astronomy, University College London, Gower Street, London WC1E 6BT, UK*
[5] *AURA for the European Space Agency, Space Telescope Science Institute, 3700 San Martin Drive, Baltimore, MD 21218, USA*
[6] *Núcleo de Astronomía, Facultad de Ingeniería y Ciencias, Universidad Diego Portales, Av. Ejército 441, Santiago, Chile*
[7] *Max Planck Institute for Astronomy, Königstuhl 17, 69117 Heidelberg, Germany*
[8] *Scuola Normale Superiore, Piazza dei Cavalieri 7, I-56126 Pisa, Italy*
[9] *Leiden Observatory, Leiden University, NL-2300 RA Leiden, Netherlands*
[10] *Department of Physics, University of Oxford, Denys Wilkinson Building, Keble Road, Oxford OX1 3RH, UK*

Accepted —. Received —; in original form —

ABSTRACT
We present new [O III] 88 μm observations of five bright $z \sim 7$ Lyman-break galaxies spectroscopically confirmed by ALMA through [C II] 158 μm, unlike recent [O III] detections where Lyman-α was used. This nearly doubles the sample of Epoch of Reionisation galaxies with robust (5σ) [C II] and [O III] detections. We perform a multi-wavelength comparison with new deep *HST* images of the rest-frame UV, whose compact morphology aligns well with [O III] tracing ionised gas. By contrast, we find more spatially extended [C II] emission likely produced in neutral gas, as indicated by a [N II] 205 μm non-detection in one source. We find a correlation between the optical [O III] + Hβ equivalent width and [O III]/[C II], as seen in local metal-poor dwarf galaxies. CLOUDY models of a nebula of typical density harbouring a young stellar population with a high ionisation parameter adequately reproduce the observed lines. Surprisingly, however, our models fail to reproduce the strength of [O III] 88 μm, unless we assume an α/Fe enhancement and near-solar nebular oxygen abundance. On spatially resolved scales, we find [O III]/[C II] shows a tentative anti-correlation with infrared excess, $L_{\mathrm{IR}}/L_{\mathrm{UV}}$, also seen on global scales in the local Universe. Finally, we introduce the far-infrared spectral energy distribution fitting code MERCURIUS to show that dust-continuum measurements of one source appear to favour a low dust temperature and correspondingly high dust mass. This implies a high stellar metallicity yield and may point towards the need of dust production or grain-growth mechanisms beyond supernovae.

Key words: galaxies: high-redshift – dark ages, reionization, first stars – methods: observational – submillimetre: ISM – techniques: imaging spectroscopy – ISM: dust

1 INTRODUCTION

The Epoch of Reionisation (EoR) marks a critical turning point in the early Universe and its study is one of the frontiers in modern astrophysics. During the EoR, the first galaxies emerged and started to rapidly form stars, which in turn began to ionise the surrounding gas – first the interstellar medium (ISM), and eventually the intergalactic medium (IGM; Dayal & Ferrara 2018; Robertson 2021). Compared to their present-day counterparts, these galaxies have not had much time to build up an abundance of metals (e.g. Maiolino & Mannucci 2019). This suggests they have metal-poor stellar populations, which results in an enhanced output of ultraviolet (UV) photons due to the hardened spectra of O- and B-type stars, in addition to containing a reduced amount of dust, implying these early

---

★ E-mail: jnw30@cam.ac.uk
† E-mail: r.smit@ljmu.ac.uk

galaxies generally experience less absorption of UV radiation (Stark 2016).

Regions where star formation takes place, especially in the very early Universe, therefore harbour stellar radiation fields with a strong intrinsic flux of ionising UV photons. Deep broadband surveys in the optical and infrared (IR) by the *Hubble Space Telescope* (*HST*) have indeed proven an effective method of finding star-forming EoR galaxies via their rest-frame UV emission, having identified a considerable number through the Lyman-break technique (currently nearly 2000 candidates at $z \geq 6$; see e.g. Bouwens et al. 2021).

Even at the earliest stages of galaxy evolution, however, dust can be of major influence. Dust grains not only catalyse star formation through the formation of molecules (Chen et al. 2018) and fragmentation of gas (Schneider et al. 2006), but they also obscure our view of these UV-bright star-forming regions. Dust is able to absorb a significant proportion of stellar optical and UV light, re-emitting the absorbed energy as thermal IR radiation. It therefore poses observational challenges to the inference of star formation rates (SFRs) solely from UV and optical measurements (Kennicutt & Evans 2012; Madau & Dickinson 2014; Bouwens et al. 2020). Indeed, recent work renewed attention on an existing notion (Hodge & da Cunha 2020): that a non-trivial fraction of high-redshift galaxies ($z \gtrsim 4$) may be so-called "*HST*-dark" systems which, even in the deepest *HST* imaging (reaching $H \sim 27$ mag), appear completely obscured at observed optical and near-infrared (NIR) wavelengths (Franco et al. 2018; Williams et al. 2019; Wang et al. 2019; Fudamoto et al. 2021; Casey et al. 2021; Manning et al. 2022). But while dust complicates the interpretation in the rest-frame UV and optical, its thermal emission also serves as a probe of the mass of the ISM (e.g. Scoville et al. 2017).

In recent years, the Atacama Large Millimeter/submillimeter Array (ALMA) has opened a new observational window for the study of star-forming galaxies at high redshift (see Hodge & da Cunha 2020 for a review). ALMA is uniquely positioned to observe their far-infrared (FIR) emission at (sub)millimetre wavelengths, which serves a twofold purpose. First, these efforts allow ALMA to directly detect the dust continuum emission. The first explorations of the FIR spectral energy distribution (SED) of galaxies in the EoR with ALMA indicate that they may rapidly build up considerable amounts of dust (e.g. Watson et al. 2015; Laporte et al. 2017). Second, nebular emission lines enable crucial spectroscopic redshift confirmations and offer valuable insights into ISM conditions by probing, for instance, the ionisation state, metal enrichment, and kinematics of the gas (see Kewley et al. 2019 for a review).

Nebular line emission typically arises in gas surrounding hot and massive stars. Gas in close vicinity forms a photoionised H ii region populated by species with an ionisation potential higher than hydrogen (e.g. O^{2+}, which requires ~ 35 eV to form), whereas shielded gas further out will contain low-ionisation species such as C^{+} (the ionisation potential of neutral carbon, 11.3 eV, is just below that of hydrogen, 13.6 eV; Abel et al. 2005). These regions can transition into photodissociation regions (PDRs) – defined as mostly neutral gas where UV photons still play a significant role in the chemistry and/or heating – in which carbon is partly photoionised (instead of hydrogen, as in H ii regions; Hollenbach & Tielens 1999). The variety of ionised and neutral gas reservoirs comprising the ISM can be traced by the many ISM coolants in the FIR, notably the [C ii] 158 μm and [O iii] 88 μm fine-structure lines ([C ii] and [O iii] hereafter; see e.g. Hashimoto et al. 2019; Katz et al. 2019; Pallottini et al. 2019; Harikane et al. 2020; Bouwens et al. 2022). [O iii] is almost exclusively produced in H ii regions, while [C ii] emission can arise in both H ii regions and PDRs. Other FIR emission lines further complement the picture: for instance, the [N ii] 205 μm transition is a powerful proxy of the ionisation state of hydrogen in the [C ii]-producing ISM (e.g. Nagao et al. 2012; Decarli et al. 2014).

The [C ii] and [O iii] lines shift into high-frequency coverage of ALMA with sufficient atmospheric transmission (i.e. band 8) above redshifts $z \sim 2.8$ and $z \sim 5.8$, respectively. For galaxies in the EoR, where ground-based observing facilities are restricted to spectroscopic studies of weaker rest-frame UV lines such as the C iii] λ 1907, [C iii] λ 1909 Å doublet (e.g. Topping et al. 2021), observations of the [C ii] and [O iii] with ALMA have first of all proven an effective spectroscopic confirmation tool, with almost as many UV-bright galaxies at $z > 6.5$ now having been spectroscopically confirmed via the [C ii] line as with H i Lyman-α (Lyα; Bouwens et al. 2022). Moreover, the [O iii] and [C ii] lines offer a powerful way of exploring ISM properties at high redshift, even in "normal" star-forming galaxies (i.e. SFR $\lesssim 100\,\mathrm{M_\odot\,yr^{-1}}$).[1] Finally, owing to its interferometric nature, ALMA produces spatially resolved spectroscopic measurements, in contrast to unresolved slit spectroscopy, which additionally faces the undesirable effect of slit losses.

In local starburst galaxies, [C ii] is observed to be the dominant FIR line, while in metal-poor dwarfs [O iii] takes over this role ($L_{[\mathrm{OIII}]}/L_{[\mathrm{CII}]} > 1$; e.g. Harikane et al. 2020). Critically, a large filling factor of diffuse, ionised gas emitting [O iii] 88 μm means metal-poor systems have a more porous ISM through which ionising radiation could "leak" (Cormier et al. 2015). The relative strengths of emission lines, in particular the [O iii] and [C ii] lines, are thus a powerful indicator of the physical state of the ISM. Interestingly, recent observations of galaxies in the EoR have systematically revealed [O iii]/[C ii] ratios similar to or even exceeding those in local metal-poor dwarf galaxies (e.g. Carniani et al. 2020).

In summary, specific properties of the ISM that can be derived from combined observations of line and continuum emission with ALMA include the dust mass and temperature, probed through its thermal emission (e.g. Bakx et al. 2020, 2021; Schouws et al. 2022b), as well as the temperature, density, ionisation (e.g. Ferrara et al. 2019; Pallottini et al. 2019; Vallini et al. 2021), metal enrichment (e.g. Vallini et al. 2015), and gas kinematics (e.g. Jones et al. 2021), all of which can be inferred from emission line strengths and spectral profiles. In turn, a robust understanding of the ISM conditions in typical EoR star-forming galaxies – that is, both of their dust and gas content – is crucial in constructing a complete physical picture of star formation in this earliest epoch and therefore also of the process of cosmic reionisation.

The main aim of this work is to analyse ALMA observations of the [C ii] 158 μm, [O iii] 88 μm, [N ii] 205 μm, and underlying dust continuum emission for a sample of five luminous, star-forming Lyman-break galaxies (LBGs) at $z \sim 7$. Specifically, we present new observations of the [O iii] 88 μm line with ALMA in addition to new *HST* imaging, which significantly increases the number of EoR sources detected in both [C ii] and [O iii] (currently 9, while only 5 have detections of at least 5σ in both lines; Carniani et al. 2020). Moreover, the sample considered in this work arguably has a weaker selection bias since, in contrast to the existing studies, all galaxies have previously been spectroscopically confirmed through [C ii] instead of Lyα. Before reionisation is completed, the latter

---

[1] For example, Smit et al. (2018) presented [C ii] detections of two $z \sim 7$ photometric galaxy candidates using a combined on-source time of less than an hour, while typical spectroscopic observations of rest-frame UV lines require multiple hours of integration time on a 10 m-class telescope.

Table 1. Sources studied in this work (colours for reference). Coordinates are given as right ascension ($\alpha_{\rm J2000}$), declination ($\delta_{\rm J2000}$), and redshift (z). These are followed by general properties of the galaxies: the apparent magnitude ($m_{\rm UV}$) and luminosity ($L_{\rm UV}$) of the rest-frame UV, the stellar mass (M_*), and the EW of the optical [O III] and Hβ lines, EW([O III] + Hβ), as presented in the works by Smit et al. (2015, 2018) and Schouws et al. (2022a,b).

Source	$\alpha_{\rm J2000}$ (h)	$\delta_{\rm J2000}$ (deg)	z	$m_{\rm UV}$ (mag)	$L_{\rm UV}$ (10^{11} L$_\odot$)	M_* (10^9 M$_\odot$)	EW([O III] + Hβ) (Å)
COS-2987030247	10:00:29.8700	02:13:02.470	6.8076	24.8 ± 0.1	1.3 ± 0.1	$1.70^{+0.49}_{-0.18}$	1128^{+166}_{-166}
COS-3018555981	10:00:30.1850	02:15:59.810	6.8540	24.9 ± 0.1	1.1 ± 0.1	$1.38^{+0.71}_{-0.21}$	1424^{+143}_{-143}
UVISTA-Z-001	10:00:43.3600	02:37:51.300	7.0611	23.9 ± 0.1	2.9 ± 0.1	$3.80^{+0.88}_{-2.10}$	1004^{+442}_{-206}
UVISTA-Z-007	09:58:46.2100	02:28:45.800	6.7498	24.5 ± 0.1	1.5 ± 0.2	$3.72^{+4.60}_{-2.37}$	761^{+530}_{-168}
UVISTA-Z-019	10:00:29.8900	01:46:46.400	6.7544	25.1 ± 0.2	1.0 ± 0.1	$3.24^{+1.78}_{-1.10}$	628^{+226}_{-99}

Table 2. Overview of ALMA observations of the five $z \sim 7$ galaxies. For each emission line observed, the observed frequency ($\nu_{\rm obs}$), total on-source integration time ($t_{\rm int}$), and channel width ($\Delta\nu_{\rm obs}$) are shown. The first indicated beam size, $A_{\rm beam}$ (given as the FWHMs of the major and minor axes), is the one tuned to match the beam between [C II] and [O III] as closely as possible, which is achieved by the listed weighting scheme of either natural or Briggs weighting, an (optional) uv taper, and the robust parameter (for Briggs weighting; see also Section 2.2.2). The second beam size indicated for a line is one using natural weighting without tapering. The RMS noise (per channel of the given width) in naturally weighted images is shown in the second to last column, in good agreement with the theoretically predicted sensitivity (in brackets) computed for use in the TCLEAN task (Section 2.2.2). The final column lists the ALMA project codes (Section 2.2.1).

Source	Emission line	$\nu_{\rm obs}$ (GHz)	$t_{\rm int}$ (h)	$\Delta\nu_{\rm obs}$ (MHz)	Weighting scheme: $A_{\rm beam}$	RMS (sensitivity) (μJy/beam)	ALMA project code(s)
COS-2987030247	[C II] 158 μm	243.429	3.6	40	Natural (0.4″): 0.7″×0.6″		2015.1.01111.S, 2018.1.01359.S
					Natural: 0.4″ × 0.4″	76.3 (89.5)	
	[O III] 88 μm	434.575	1.1	70	Briggs (0.5): 0.7″ × 0.5″		2018.1.00429.S
					Natural: 0.8″ × 0.6″	487 (548)	
	[N II] 205 μm	186.996	1.3	30	Natural: 0.8″ × 0.7″	166 (202)	2018.1.01551.S
COS-3018555981	[C II] 158 μm	241.991	14	40	Natural (0.4″): 0.6″×0.6″		2015.1.01111.S, 2017.1.00604.S
					Natural: 0.4″ × 0.4″	45.0 (48.7)	
	[O III] 88 μm	432.008	0.99	70	Briggs (0.5): 0.7″ × 0.5″		2018.1.00429.S
					Natural: 0.9″ × 0.6″	429 (456)	
UVISTA-Z-001	[C II] 158 μm	235.774	4.2	40	Natural: 0.6″ × 0.5″	234 (119)	2015.1.00540.S, 2018.1.00085.S, 2018.1.00933.S, 2019.1.01611.S
	[O III] 88 μm	420.909	1.3	70	Natural (0.2″): 0.6″×0.5″		2019.1.01524.S
					Natural: 0.5″ × 0.5″	435 (465)	
UVISTA-Z-007	[C II] 158 μm	245.244	0.44	40	Briggs (1.0): 1.3″ × 1.1″		2018.1.00085.S
					Natural: 1.4″ × 1.2″	272 (286)	
	[O III] 88 μm	437.817	1.6	70	Natural (1.0″): 1.1″×1.1″		2019.1.01524.S
					Natural: 0.6″ × 0.5″	738 (641)	
UVISTA-Z-019	[C II] 158 μm	245.099	4.4	40	Natural (0.2″): 0.4″×0.4″		2018.1.00085.S, 2019.1.01611.S
					Natural: 0.4″ × 0.3″	81.2 (92.3)	
	[O III] 88 μm	437.557	0.89	70	Briggs (1.5): 0.5″ × 0.4″		2019.1.01524.S
					Natural: 0.5″ × 0.4″	1015 (680)	

can namely only escape from galaxies occupying ionised bubbles, which are indicative of overdense regions (e.g. Leonova et al. 2021).

Our outline is as follows. Section 2 discusses the available ALMA and *HST* data and Section 3 briefly discusses the results of these observations. In Sections 4 and 5, we compare our findings concerning respectively the dust continuum and emission lines to other works in the literature and discuss our findings. Section 6 provides a summary.

In our analysis, we adopt the cosmological parameters $\Omega_{\rm m} = 0.3$, $\Omega_\Lambda = 0.7$, and $H_0 = 70\,{\rm km\,s^{-1}\,Mpc^{-1}}$ throughout (implying an angular scale of 5.2 kpc/arcsec at $z = 7$). All magnitudes are in the AB system (Oke & Gunn 1983).

2 OBSERVATIONS

2.1 Target selection

Five galaxies at $z \sim 7$, all located in the $\sim 2\,{\rm deg}^2$ UltraVISTA field (UVISTA; McCracken et al. 2012), are considered in this work: COS-2987030247, COS-3018555981, UVISTA-Z-001, UVISTA-Z-007, and UVISTA-Z-019 (Table 1). The first two, COS-2987030247 and COS-3018555981, are contained in the *HST* CANDELS field (Grogin et al. 2011) and were spectroscopically confirmed with ALMA observations of [C II] 158 μm in Cycle 3 (ALMA project code 2015.1.01111.S; Smit et al. 2018). The two sources were selected for their large optical emission line EWs, which enables an accurate photometric redshift determination using *Spitzer*/IRAC broadband photometry at 3.6 μm and 4.5 μm (see Smit et al. 2015 for details). The EWs of the optical [O III] (notably at 4960 Å and 5008 Å) and Hβ lines (hereafter simply EW([O III] + Hβ)), presented in Smit et al. (2015), are

EW([O III] + Hβ) > 1000 Å, while the median EW at $z \sim 7$ is around 1000 Å (see e.g. Endsley et al. 2021). All five sources are bright in the UV, with apparent magnitudes between 24 and 25 mag, implying $L_{\mathrm{UV}} \sim 2L^*_{\mathrm{UV}}(z \sim 7)$. SED fitting with a Chabrier (2003) initial mass function (IMF) yields stellar masses between 1 and 4 times 10^9 M$_\odot$ (Smit et al. 2018; Schouws et al. 2022b; see Table 1).

The precise photometric redshift allowed ALMA to perform efficient blind spectral scans to search for the [C II] line without first requiring a spectroscopic confirmation through Lyα. Its success encouraged a second programme in Cycle 6 (2018.1.00085.S; Schouws et al. 2022a) that has successfully detected the [C II] line in three out of six additional galaxies, selected from ground-based imaging in the wider COSMOS field. Among these are the latter three sources considered here (UVISTA-Z-001, UVISTA-Z-007, and UVISTA-Z-019), two of which in comparison have modest EWs (presented in Schouws et al. 2022a), EW([O III] + Hβ) ∼ 600-700 Å, more typical for UV-bright LBGs at $z \sim 7$ (e.g. Endsley et al. 2021). For an in-depth description of ALMA target selection strategies and scanning efficacy of [C II] we refer to Bouwens et al. (2022), introducing the successor of these two pilot programmes, the Reionization Era Bright Emission Line Survey (REBELS). This ALMA Large Program has targeted [C II] and [O III] in 40 of the brightest UV-selected star-forming galaxy candidates at $z > 6.5$.

2.2 ALMA data

An overview of the ALMA observations considered in this work is shown in Table 2. In the following sections, we will briefly describe the existing ALMA observations of the [C II] 158 μm line, and the data reduction process of new measurements of the [O III] 88 μm and [N II] 205 μm lines and the underlying dust continuum.

2.2.1 *ALMA programmes used in this study*

In this study, we consider three main follow-up programmes of the bright LBGs that were confirmed with [C II] described in Section 2.1. COS-2987030247 was observed in band 5, targeting the [N II] 205 μm line with programme 2018.1.01551.S in Cycle 6 (note that for COS-3018555981 [N II] 205 μm falls into the atmospheric feature at the centre of band 5 and could not be included in this programme). All five bright [C II] emitting galaxies described in Section 2.1, were approved for A-ranked observations in band 8 in Cycle 6 (project code 2018.1.00429.S) and 7 (2019.1.01524.S) for the CANDELS-COSMOS and UVISTA sources, respectively.

Finally, we also make use of additional [C II] data that was taken at high angular resolution ($\theta_{\mathrm{beam}} < 0.2''$), co-adding these with the low-resolution data for all sources except UVISTA-Z-007 (2017.1.00604.S, 2018.1.01359.S, 2019.1.01611.S). Similarly, we include additional band-6 observations of the dust continuum in UVISTA-Z-001 (2015.1.00540.S, 2018.1.00933.S) presented in Bowler et al. (2018, 2022).

2.2.2 *ALMA data reduction*

All data, including previous observations discussed above (see Table 2), were calibrated and reduced with the automated pipeline of the Common Astronomy Software Application (CASA; McMullin et al. 2007) version 5.6 (with the exception of 2015.1.00540.S and 2015.1.01111.S, which required version 4.7).

Before the imaging step, we performed the UVCONTSUB task to separate the continuum and line visibilities specifically for imaging the [C II] emission in COS-3018555981, UVISTA-Z-001, and UVISTA-Z-019 as well as the [O III] emission in UVISTA-Z-001, where the underlying dust continuum is confidently detected (Section 3.1; see also Schouws et al. 2022b). Images were made with the TCLEAN task for a large range of parameter sets, using all available data sets combined. We created images using both natural and Briggs weightings; under the natural weighting scheme, several different uv tapers were considered as well as no taper. For measuring the total [O III] and [C II] line fluxes, a moderately (0.6″) tapered image was chosen to avoid resolving out extended emission (see e.g. Carniani et al. 2018a, 2020) as best as possible while maintaining a good signal-to-noise ratio (SNR). However, a natural weighting without any tapering was considered for the [N II] line to maximise the SNR. Continuum images were created by averaging (i.e. the MFS mode in TCLEAN) over all available spectral channels that were well outside the relevant emission line range (i.e. $|v| > 1000$ km/s). Natural weighting was again used for optimal SNR, however given the heterogeneity of the ALMA data, the following tapers were applied on a case-by-case basis to match the beams across various bands: 0.4″ for the band-6 data of COS-2987030247, 0.6″ for the band-6 data of COS-3018555981, 0.8″ for the band-8 data of UVISTA-Z-001, 1.0″ for the band-8 data of UVISTA-Z-007, and 0.2″ for the band-6 data of UVISTA-Z-019.

Finally, when comparing the [C II] and [O III] lines, we also tuned the weighting or taper scheme to match the beam sizes as closely as possible. We use Briggs weighting for the line observed with lowest spatial resolution with a robust parameter tuned to the highest resolution achievable while maintaining a reasonable SNR. The other line is imaged with natural weighting and, if required, a small taper. Table 2 lists the resulting matched beam sizes for [C II] and [O III] (as well as beam sizes obtained with an untapered, natural-weighting scheme). Furthermore, the measured root-mean-square (RMS) noise in naturally weighted images is compared in Table 2 to the theoretically expected value of the sensitivity of an interferometric image (Thompson et al. 2017),[2]

$$\delta S_\nu = \frac{2 k_{\mathrm{B}} T_{\mathrm{sys}}}{A_{\mathrm{eff}} \sqrt{N_{\mathrm{ant}} (N_{\mathrm{ant}} - 1) t_{\mathrm{int}} \Delta\nu}}, \tag{1}$$

where k_{B} is the Boltzmann constant, N_{ant} is the number of antennas (where we take the mean if observations obtained with multiple configurations are combined), t_{int} is the total on-source integration time, $\Delta\nu$ is the channel width, T_{sys} is the system temperature, and A_{eff} is the effective collective area of each dish. Given the dish radius r_{ant},

$$A_{\mathrm{eff}} = \eta \pi r_{\mathrm{ant}}^2,$$

which is equal to ∼ 80 m^2 for the 12-meter ALMA antennae assuming an efficiency factor of $\eta \sim 0.7$ (Cortes et al. 2020). These sensitivities, which agree well with the empirically measured RMS noise, were computed for use in the TCLEAN task, where the threshold parameter was set to three times this value.

2.3 *HST* imaging

For sources at a redshift of $z \sim 7$, the rest-frame UV is observed in the NIR, ideally suited for observations with the infrared channel of

---

[2] We note this is a simplified formula which leaves out a few additional system efficiencies; see Section 9.2.1 of the ALMA Technical Handbook (Cortes et al. 2020) for a more detailed form.

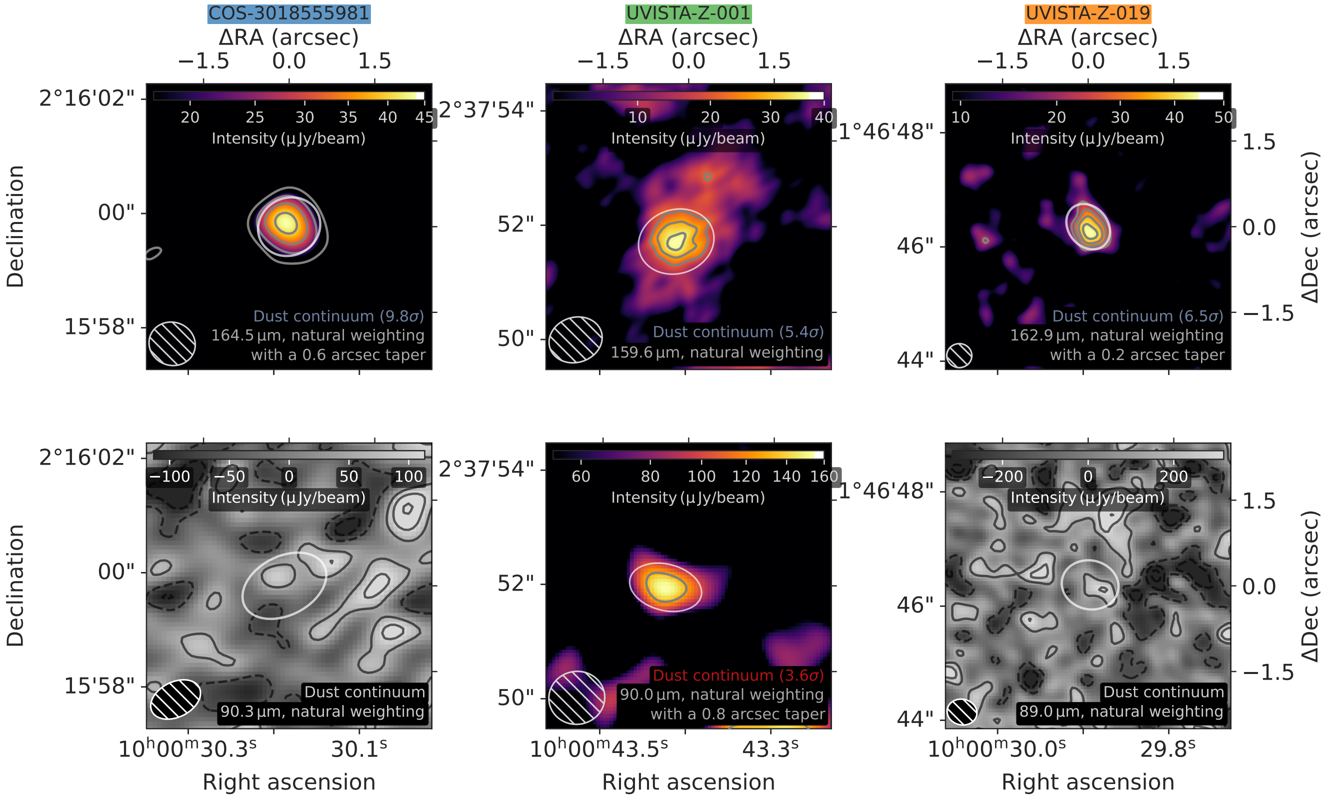

Figure 1. Naturally weighted dust continuum maps of COS-3018555981 (first column), UVISTA-Z-001 (second column), and UVISTA-Z-019 (third column); beam sizes are indicated in the bottom left. Top row: clear detections at $\lambda_{\rm emit} \sim 160\,\mu$m (imaged with varying degrees of taper; see Sections 2.2.2 and 3.1). Grey contours show subsequent significance levels in steps of 2σ (COS-3018555981) or 1σ (UVISTA-Z-001 and UVISTA-Z-019), starting at 3σ. White ellipses show the two-dimensional Gaussian fit obtained by IMFIT procedure in CASA. Bottom row: (non-)detections at $\lambda_{\rm emit} \sim 90\,\mu$m. Contours are the same as the top row for UVISTA-Z-001, otherwise solid (dashed) grey lines show positive (negative) 1σ, 2σ, and 3σ contours and white ellipses show the aperture used for determining a flux density upper limit (Section 3.1). Since there is significant extended emission at $\sim 160\,\mu$m in UVISTA-Z-001, the white ellipses show the aperture used to measure the flux of the compact component in both the top and bottom panels (Section 3.1).

the Wide Field Camera 3 (WFC3) on board *HST*. For the two sources in the COSMOS field, COS-2987030247 and COS-3018555981, *HST* imaging is available in the F125W (J_{125}), F140W (JH_{140}), and F160W (H_{160}) filters as part of CANDELS (GO 12440, PI: Faber) and the 3D-HST Treasury Programs (GO 12328, PI: Van Dokkum).[3] Combined, these observations reach a median depth of 26.1 mag, 25.5 mag, and 25.8 mag (5σ for a $1''$-diameter aperture) in the J_{125}, JH_{140}, and H_{160} bands, respectively (Grogin et al. 2011; Koekemoer et al. 2011; Skelton et al. 2014). Throughout this work, we use a single stacked image, created by weighting the three filters by their inverse variance (covering $1400\,\text{Å} \lesssim \lambda_{\rm emit} \lesssim 2200\,\text{Å}$). For UVISTA-Z-001, we use *HST* imaging in the F140W filter (GO 13793, PI: Bowler) presented in Bowler et al. (2017).[4]

For COS-2987030247, we manually remove a foreground source to the north-west. The foreground source is offset by just under $1''$ and clearly (above 5σ) detected in the Advanced Camera for Surveys (ACS) F606W and F814W filters, while for sources at $z \sim 6.8$, the IGM would absorb any emission below the Lyman-continuum limit at a rest-frame wavelength of 912 Å (observed at $\sim 0.7\,\mu$m). In our stacked image, we replaced pixels with artificial noise if they are detected above 4σ in a weighted ACS image that has been smoothed to match the slightly more extended point spread function (PSF) of WFC3.

In addition, *HST* observations to acquire rest-frame UV imaging of UVISTA-Z-007 and UVISTA-Z-019 were awarded in Cycle 28 in the Mid-Cycle General Observer programme ID 16506 (PI: Witstok).[5] Observations were performed with WFC3 using the F140W (JH_{140}) filter with a 5 ks exposure per target, motivated by the goal of properly resolving the spatial substructure of the rest-frame UV. We divided each orbit into 4 exposures, which allows for a four-point dithering pattern to improve sampling of the PSF and to remove bad pixels, cosmic ray impacts, and detector artefacts. We used the SPARS50 sampling sequence with NSAMP = 13 and NSAMP = 14 in two subsequent orbits for both targets.

Calibrated data products were combined using the AstroDrizzle task (e.g. Fruchter & Hook 2002) within the DrizzlePac package[6] setting the FINAL_PIXFRAC parameter to 0.8 and choosing a pixel size of $0.065''$. The resulting images reach a 5σ depth of 27.7 mag for a $0.5''$-diameter aperture (i.e. 25.9 mag/arcsec^2).

The astrometry of all images was calibrated to *Gaia* data (Gaia

---

[3] High-level science products are available on `https://archive.stsci.edu/prepds/3d-hst/`.

[4] Data may be obtained from the MAST at 10.17909/6gya-3b10.

[5] Data may be obtained from the MAST at 10.17909/T9-JHSF-M392.

[6] See `https://www.stsci.edu/scientific-community/software/drizzlepac.html`.

Collaboration et al. 2016, 2021) by fitting a two-dimensional Gaussian to the *HST* images of a number of nearby stars with a g-band magnitude of $g \lesssim 21$ mag (7, 5, 6, 4, and 2 for COS-2987030247, COS-3018555981, UVISTA-Z-001, UVISTA-Z-007, and UVISTA-Z-019, respectively). Among the stars in each field, we found the measured peak offsets relative to *Gaia* positions agreed very well within less than 0.05″; taken together, they resulted in a required median correction of less than about 0.1″ in all cases.

3 RESULTS

3.1 Dust continuum

Except for a $\sim 4\sigma$ detection in UVISTA-Z-001, the dust continuum at a rest-frame wavelength of $\lambda_{\mathrm{emit}} \sim 90\,\mu\mathrm{m}$ remains undetected for the other sources. The same holds for the dust continuum of COS-2987030247 around the [N II] line at 205 µm. The continuum at $\lambda_{\mathrm{emit}} \sim 160\,\mu\mathrm{m}$, however, is detected in COS-3018555981, UVISTA-Z-001, and UVISTA-Z-019 (see also Schouws et al. 2022b; Bowler et al. 2022). Dust continuum maps of these sources are shown in Figure 1.

For consistency in the flux measurements across different ALMA bands, their beams are matched by applying a slight taper to higher resolution data (see Section 2.2.2). For COS-3018555981 and UVISTA-Z-019, we place 3σ upper limits at ~ 90 µm by empirically measuring the RMS noise in a beam-shaped aperture matched in (convolved) size to the source extent at ~ 160 µm; for COS-2987030247 and UVISTA-Z-007, a (FWHM) beam-sized aperture is used. Since there is significant extended emission at ~ 160 µm in UVISTA-Z-001, we measure fluxes of the compact component in an aperture centred on the peak of the emission and matched in (convolved) size to the source extent at ~ 90 µm (implications for the inferred dust properties will be discussed in Section 4). In estimating the uncertainties on our continuum detections as well as upper limits, we conservatively take a systematic flux calibration uncertainty into account (10% in band 5 and 6, 20% in band 8).[7]

In Table 3, all continuum measurements around the three emission lines (including A_{dust}, the deconvolved source extent in kpc^2, if detected) are summarised. Also presented in Table 3 are other characteristics of the sources like their corresponding total IR and FIR luminosities (defined as the integrated luminosity between 8 and 1000 µm and between 42.5 and 122.5 µm in the rest frame, respectively; see e.g. Reuter et al. 2020) and other dust properties, leveraging constraints from the combined continuum measurements. These properties have been derived from a best-fit "greybody" spectrum (e.g. Casey et al. 2014) if possible and will be discussed in more detail in Section 4. When only upper limits are available (i.e. for COS-2987030247 and UVISTA-Z-007; see Section 4.1), we report 3σ upper limits on the IR and FIR luminosities by assuming a fiducial $\beta_{\mathrm{IR}} = 1.5$ and $T_{\mathrm{dust}} = 50$ K; we acknowledge the uncertainty on these parameters by adding an additional 0.4 dex systematic uncertainty to the integrated luminosities and corresponding obscured SFR (cf. Carniani et al. 2020) before setting upper limits.

3.2 [N II] 205 µm

We placed a 3σ upper limit on the [N II] luminosity of COS-2987030247 by first measuring the RMS noise in the untapered, naturally-weighted datacube over a single beam (assuming the source is unresolved). We obtained an upper limit on the line flux in Jy km/s by scaling this noise to a range of channels covering twice the maximum FWHM between the [O III] and [C II] lines (Section 3.3), which we then converted to a luminosity, as shown in Table 4. The lower limit on the [C II] 158 µm to [N II] 205 µm ratio is $L_{[\mathrm{C\,II}]}/L_{[\mathrm{N\,II}]} > 4.8$ (3σ).

3.3 [O III] 88 µm and [C II] 158 µm

We obtained moment-zero maps by integrating a naturally weighted, clean datacube over the FWHM around the line centre. Defining the SNR as that measured for the peak pixel, the [O III] and [C II] lines are detected with a significance of at least SNR > 5 in all five sources. Total line fluxes, however, are measured on cleaned cubes with a 0.6″ taper to recover extended emission as well as possible (Section 2.2.2), integrating all channels where line flux is detected (coloured channels in Figure 2) in a spectrum extracted from a contiguous region of spaxels reaching at least 2σ in the moment-zero map, the spectrum each spaxel weighted by its SNR. In turn, this initial moment-zero map was created by integrating channels within half of the FWHM from the line centre (used in the SNR determination described above). Again, we take a conservative systematic flux calibration uncertainty into account, as discussed in Section 3.1. The resulting line fluxes, luminosities, and ratios are listed in Table 4.

4 DUST PROPERTIES

Although accounting for only a small fraction of baryonic matter in galaxies, dust is highly relevant in the context of galaxy evolution (e.g. Liang et al. 2019). Representative dust properties of EoR galaxies, however, are still difficult to constrain with current observations partly due to the degeneracy between dust mass and temperature, complicated further by the dust opacity. Only in a few cases, multiple constraints on the FIR SED of normal star-forming galaxies ($\mathrm{SFR} \lesssim 100\,\mathrm{M_\odot\,yr^{-1}}$) in the EoR are available (e.g. Hashimoto et al. 2019; Bakx et al. 2020, 2021). Here, we use the available band-6 detections in combination with the non-detections in band 8 to obtain further insights into the (F)IR luminosity, $L_{\mathrm{(F)IR}}$, corresponding obscured and total SFR,[8] dust mass (Section 4.2), and dust temperature (Section 4.3) of typical UV-bright EoR galaxies.

4.1 Dust SED fitting procedure

A dust-continuum detection at $\lambda_{\mathrm{emit}} \sim 160$ µm combined with a detection (UVISTA-Z-001) or even an upper limit (COS-3018555981 and UVISTA-Z-019) at $\lambda_{\mathrm{emit}} \sim 90$ µm can provide insight into the dust properties beyond those derived with a fixed temperature, emissivity, and opacity model. To investigate this in detail, we performed a fitting routine using the multimodal nested sampling algorithm MULTINEST (described in Feroz et al. 2009) implemented in PYTHON as the PYMULTINEST package (Buchner et al. 2014), as described below. The full code of this routine which treats detections and upper limits uniformly and we therefore refer to as MERCURIUS (Multimodal Estimation Routine for the Cosmological Unravelling of Rest-frame Infrared Uniformised Spectra), is available online.[9]

---

[7] See Section A.9.2 of the ALMA Proposers' Guide (Braatz et al. 2021).

[8] Obtained from the UV and IR luminosities using the conversions in Kennicutt & Evans (2012).

[9] See `https://github.com/joriswitstok/mercurius/`.

Table 3. Average, minimum, and maximum channel rest-frame wavelength and observed frequency used for the aggregate continuum images and corresponding (upper limits on) continuum fluxes. For non-detections, 3σ upper limits are given (with theoretical 3σ sensitivities, given by equation (1), in brackets). For detections, deconvolved sizes $A_{\rm dust}$ as measured by the CASA IMFIT procedure are given. Dust-related quantities listed are the mass $M_{\rm dust}$, mass surface density $\Sigma_{\rm dust}$, and yield $y_{\rm dust}$, discussed in Section 4.2; the intrinsic SED temperature $T_{\rm dust}$ and peak temperature $T_{\rm peak}$, discussed in Section 4.3; the integrated IR and FIR luminosities ($L_{\rm (F)IR}$); and finally, the obscured and total SFRs, $\rm SFR_{IR}$ and $\rm SFR_{tot}$. These properties are inferred from MERCURIUS fits where possible (i.e. for COS-3018555981, UVISTA-Z-001, and UVISTA-Z-019), under the fiducial self-consistent opacity model (for a more in-depth discussion, see Section 4.1). Otherwise, they are approximated under a fully optically thin SED with the fiducial assumptions of $T_{\rm dust} = 50\,{\rm K}$, $\beta_{\rm IR} = 1.5$, which however introduces large systematic uncertainties (see Section 3.1 for details). For COS-3018555981, an upper limit (95% confidence) on the dust temperatures is reported in brackets.

Regime	Quantity	COS-2987030247	COS-3018555981	UVISTA-Z-001	UVISTA-Z-007	UVISTA-Z-019
Band 8	$\nu_{\rm obs}$ (GHz)	$426.2^{+9.3}_{-6.7}$	$422.5^{+8.4}_{-5.4}$	$413.0^{+8.9}_{-6.9}$	$434.5^{+6.2}_{-7.7}$	$434.4^{+6.1}_{-7.8}$
	$\lambda_{\rm emit}$ (μm)	$90.1^{+1.4}_{-1.9}$	$90.3^{+1.2}_{-1.8}$	$90.0^{+1.5}_{-1.9}$	$89.0^{+1.6}_{-1.3}$	$89.0^{+1.6}_{-1.2}$
	$S_{\nu,\,\rm obs}$ (μJy)	< 163 (160)	< 210 (240)	189 ± 100	< 361 (260)	< 840 (625)
	$A_{\rm dust}$ (kpc^2)	. . .	. . .	$(5.2 \pm 2.4)\times$ (2.0 ± 1.3)	. . .	. . .
Band 6	$\nu_{\rm obs}$ (GHz)	$250.3^{+7.3}_{-9.8}$	$232.1^{+13.3}_{-8.0}$	$232.9^{+10.0}_{-16.0}$	$242.4^{+2.0}_{-2.1}$	$237.3^{+8.8}_{-11.0}$
	$\lambda_{\rm emit}$ (μm)	$153.4^{+6.2}_{-4.4}$	$164.5^{+5.9}_{-8.9}$	$159.6^{+11.8}_{-6.6}$	$159.6^{+1.4}_{-1.3}$	$162.9^{+7.9}_{-5.8}$
	$S_{\nu,\,\rm obs}$ (μJy)	< 22.5 (18.4)	76 ± 13	97 ± 30	< 69.6 (81.8)	131 ± 36
	$A_{\rm dust}$ (kpc^2)	. . .	$(4.3 \pm 0.8)\times$ (3.6 ± 0.7)	$(10.3 \pm 3.4)\times$ (3.7 ± 3.0)	. . .	$(4.1 \pm 1.1)\times$ (3.0 ± 0.9)
Band 5	$\nu_{\rm obs}$ (GHz)	$195.6^{+6.4}_{-9.4}$	. . .	. . .	. . .	. . .
	$\lambda_{\rm emit}$ (μm)	$196.3^{+9.9}_{-6.3}$	. . .	. . .	. . .	. . .
	$S_{\nu,\,\rm obs}$ (μJy)	< 19.4 (22.8)	. . .	. . .	. . .	. . .
	$T_{\rm dust}$	Fixed: 50 K	MERCURIUS fit	MERCURIUS fit	Fixed: 50 K	MERCURIUS fit
	λ_0 (opacity)	Optically thin	Self-consistent: $8.4^{+11.8}_{-4.4}$ μm	Self-consistent: $0.6^{+0.7}_{-0.3}$ μm	Optically thin	Self-consistent: $4.2^{+7.5}_{-2.7}$ μm
	$\beta_{\rm IR}$	Fixed: 1.5	Fixed: 1.5	Fixed: 1.5	Fixed: 1.5	Fixed: 1.5
	$M_{\rm dust}$ (M$_\odot$)	$\lesssim 4 \cdot 10^6$	$7^{+19}_{-5} \cdot 10^7$	$4^{+8}_{-3} \cdot 10^6$	$\lesssim 1 \cdot 10^7$	$2.1^{+7.6}_{-1.6} \cdot 10^7$
	$\Sigma_{\rm dust}$ (M$_\odot$ pc^{-2})	. . .	7^{+18}_{-4}	$0.1^{+0.3}_{-0.1}$	. . .	$2.3^{+8.5}_{-1.8}$
	$M_{\rm dust}/M_*$	$\lesssim 0.002$	$0.05^{+0.16}_{-0.04}$	$0.001^{+0.003}_{-0.0007}$	$\lesssim 0.003$	$0.007^{+0.03}_{-0.006}$
	$y_{\rm dust,\,AGB}$ (M$_\odot$)	$\lesssim 0.1$	$1.5^{+4.6}_{-1.1}$	$0.03^{+0.08}_{-0.02}$	$\lesssim 0.1$	$0.2^{+0.9}_{-0.2}$
	$y_{\rm dust,\,SN}$ (M$_\odot$)	$\lesssim 0.2$	$4.5^{+13.3}_{-3.1}$	$0.09^{+0.2}_{-0.06}$	$\lesssim 0.3$	$0.6^{+2}_{-0.5}$
	$T_{\rm dust}$ (K)	. . .	29^{+9}_{-5} (< 48)	59^{+41}_{-20}	. . .	47^{+40}_{-17}
	$T_{\rm peak}$ (K)	. . .	26^{+8}_{-5} (< 43)	53^{+37}_{-17}	. . .	42^{+35}_{-15}
8-1000 μm	$L_{\rm IR}$ (L$_\odot$)	$\lesssim 2.1 \cdot 10^{11}$	$9.9^{+6.8}_{-2.3} \cdot 10^{10}$	$2.0^{+9.5}_{-1.3} \cdot 10^{11}$	$\lesssim 6.9 \cdot 10^{11}$	$3.1^{+18.1}_{-1.8} \cdot 10^{11}$
42.5-122.5 μm	$L_{\rm FIR}$ (L$_\odot$)	$\lesssim 1.4 \cdot 10^{11}$	$6.4^{+4.8}_{-1.6} \cdot 10^{10}$	$1.1^{+1.1}_{-0.6} \cdot 10^{11}$	$\lesssim 4.7 \cdot 10^{11}$	$2.1^{+4.2}_{-1.3} \cdot 10^{11}$
IR (8-1000 μm)	$\rm SFR_{IR}$ (M$_\odot$ yr^{-1})	$\lesssim 32$	15^{+10}_{-3}	30^{+142}_{-20}	$\lesssim 102$	46^{+270}_{-27}
UV + IR	$\rm SFR_{tot}$ (M$_\odot$ yr^{-1})	$\lesssim 54$	34^{+10}_{-4}	79^{+142}_{-20}	$\lesssim 128$	63^{+270}_{-27}

Table 4. Observed line fluxes ($F_{\rm line}$) of [C II] 158 μm, [O III] 88 μm, and [N II] 205 μm, given in units of Jy km/s (i.e. as $S_\nu \Delta v$; see Sections 3.2 and 3.3 for details). Also shown are corresponding line luminosities and the [O III]/[C II] luminosity ratio. For non-detections, 3σ upper limits are given.

Source	$F_{\rm [C\,II]}$ (Jy km/s)	$L_{\rm [C\,II]}$ (10^8 L$_\odot$)	$F_{\rm [O\,III]}$ (Jy km/s)	$L_{\rm [O\,III]}$ (10^8 L$_\odot$)	$L_{\rm [O\,III]}/L_{\rm [C\,II]}$	$F_{\rm [N\,II]}$ (Jy km/s)	$L_{\rm [N\,II]}$ (10^8 L$_\odot$)
COS-2987030247	0.250 ± 0.061	2.83 ± 0.69	0.79 ± 0.20	16.0 ± 4.1	5.7 ± 1.8	< 0.0679	< 0.591
COS-3018555981	0.347 ± 0.027	3.97 ± 0.31	1.58 ± 0.29	32.3 ± 5.9	8.13 ± 0.92	. . .	. . .
UVISTA-Z-001	0.564 ± 0.095	6.7 ± 1.1	0.92 ± 0.22	19.6 ± 4.7	2.91 ± 0.66	. . .	. . .
UVISTA-Z-007	0.408 ± 0.065	4.57 ± 0.73	0.65 ± 0.30	12.9 ± 5.9	2.8 ± 1.0	. . .	. . .
UVISTA-Z-019	0.686 ± 0.049	7.69 ± 0.55	0.83 ± 0.35	16.6 ± 7.0	2.16 ± 0.54	. . .	. . .

Apart from the main fitting procedure, it also includes a greybody SED exploration visualisation tool; both are illustrated in a documented example.

Radiative transfer predicts the intensity emerging from a region of dust at a temperature $T_{\rm dust}$ becomes a modified black body (often referred to as a greybody; e.g. Jones et al. 2020a),

$$J_\nu = \left(1 - e^{-\tau(\nu)}\right) B_\nu\left(T_{\rm dust}\right), \tag{2}$$

where B_ν is the Planck function (Planck 1901), a specific intensity in units of erg s^{-1} cm^{-2} sr^{-1} Hz^{-1} that is attenuated by the opacity

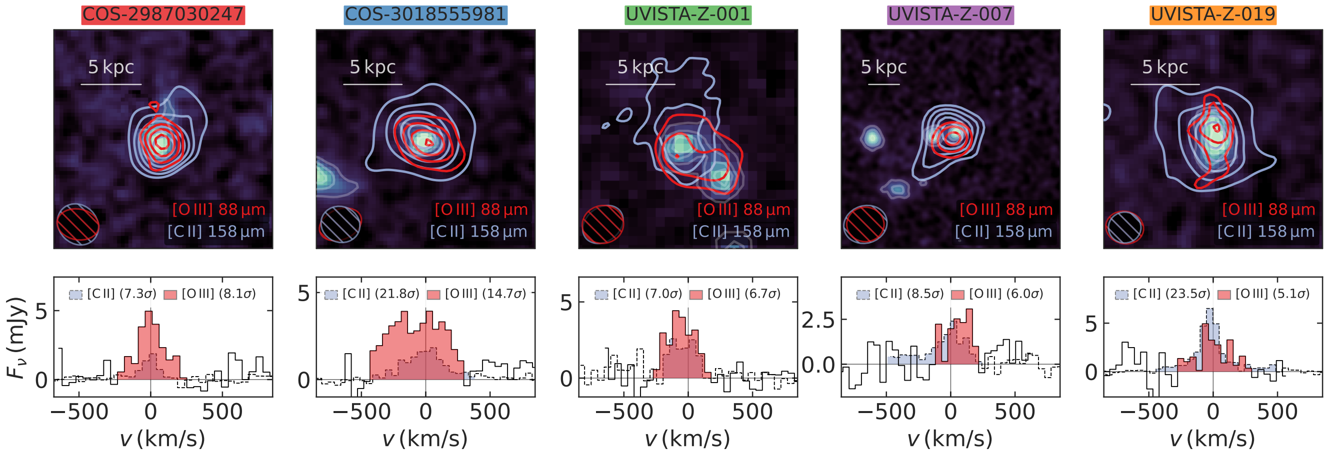

Figure 2. Detections of the [C ii] 158 μm and [O iii] 88 μm lines. Top row: contour images of the [C ii] and [O iii] lines overlaid on a background of *HST* rest-frame UV images (see Section 2.3). The line images have matched beam sizes (as listed in Table 2) and are produced by collapsing all channels within the FWHM of the line (as those of the SNR determination, which however use natural weighting without tapering; Section 3.3). Contours start at 3σ and increase in steps of 5σ for the [C ii] contours in COS-3018555981 and UVISTA-Z-019, 3σ for the [O iii] contours in COS-3018555981, 2σ for both lines in UVISTA-Z-001, and 1σ otherwise. Bottom row: SNR-weighted line spectra extracted from a 2σ region in a naturally weighted image integrated over the FWHM (cf. Section 3.3). Coloured channels, which were used to produce a subsequent moment-zero map for measuring the total line flux, indicate the line detection. The significance of each line detection is shown in the legend (also see Section 3.3 for details).

term containing the optical depth, $\tau(\nu)$. However, the observed flux needs to be corrected for the effect of observing against the isotropic Cosmic Microwave Background (CMB), which involves subtracting the Planck function for $T_{\rm CMB}(z)$, the CMB temperature at redshift z, from the dust blackbody term (as in equation (18) in da Cunha et al. 2013). The flux density observed at $\nu_{\rm obs} = \nu/(1+z)$,[10] denoted $S_{\nu,\,\rm obs}$ and given in $\rm erg\,s^{-1}\,cm^{-2}\,Hz^{-1}$, is then given by the following general form of the observed SED (see also Jones et al. 2020a),

$$S_{\nu,\,\rm obs} = \frac{A_{\rm dust}\,(1+z)}{D_L^2(z)} \left(1 - e^{-\tau(\nu)}\right) \left[B_\nu\left(T_{\rm dust}\right) - B_\nu\left(T_{\rm CMB}(z)\right)\right], \tag{3}$$

where $A_{\rm dust}$ is the area subtended by the source. In our fiducial model, the optical depth is taken to be proportional to the dust mass surface density $\Sigma_{\rm dust}$ (Casey et al. 2014) via

$$\tau(\nu) \equiv \kappa_\nu\,\Sigma_{\rm dust} = \kappa_\nu\,C\,\frac{M_{\rm dust}}{A_{\rm dust}}, \text{ with } C \geq 1. \tag{4}$$

Here, we substituted $\Sigma_{\rm dust}$ by a combination of C, a clustering factor,[11] the dust mass $M_{\rm dust}$, and $A_{\rm dust}$, which we take to be the deconvolved size of the dust emission found by the imfit procedure in casa (given in Table 3; see e.g. Figure 1). The absorption cross section (per unit mass), κ_ν, is the frequency-dependent constant of proportionality. This frequency dependence is parametrised via a power law with the dust emissivity $\beta_{\rm IR}$ as its exponent (Draine 2006),

$$\kappa_\nu = \kappa_{\nu,\,\rm ref}\left(\frac{\nu}{\nu_{\rm ref}}\right)^{\beta_{\rm IR}}. \tag{5}$$

Following Schouws et al. (2022b), we used $\kappa_{\nu,\,\rm ref} = 8.94\,{\rm cm^2\,g^{-1}}$ at $\lambda_{\rm ref} = 158\,\mu{\rm m}$ (i.e. $\nu_{\rm ref} = \nu_{\rm [C\,II]} \simeq 1.90\,{\rm THz}$), appropriate for dust ejected by supernovae (SNe) after reverse shock destruction (values for different dust grain compositions range from $5\,{\rm cm^2\,g^{-1}} \lesssim \kappa_{\nu,\,\rm ref} \lesssim 30\,{\rm cm^2\,g^{-1}}$; see Hirashita et al. 2014, and references therein). As will be discussed in Section 4.2, SNe are the most likely origin of dust in these young, metal-poor star-forming galaxies. However, since the detailed dust composition is in principle unknown, $\kappa_{\nu,\,\rm ref}$ carries with it a systematic uncertainty that can lower dust masses by $\sim 3\times$ or increase them by $\sim 1.5\times$.

For convenience, the optical depth can be expressed in the form

$$\tau(\nu) = \left(\frac{\nu}{\nu_0}\right)^{\beta_{\rm IR}} = \left(\frac{\lambda_0}{\lambda}\right)^{\beta_{\rm IR}}, \tag{6}$$

which clearly marks the point at which the dust transitions from optically thin to thick, at $\lambda_0 = c/\nu_0$. For LBGs at high redshift, λ_0 is typically assumed to be well below the sampled wavelength regime so that it is safe to approximate the entire SED as being optically thin ($\tau(\nu) \ll 1$; e.g. Bakx et al. 2021) which simply reduces equation (3) to

$$S_{\nu,\,\rm obs} = M_{\rm dust}\,\frac{1+z}{D_L^2(z)}\,\kappa_\nu\left[B_\nu\left(T_{\rm dust}\right) - B_\nu\left(T_{\rm CMB}(z)\right)\right]. \tag{7}$$

However, this assumption can lead to a significantly underestimated dust temperature and overestimated dust mass if incorrectly applied on measurements that sample a region where the approx-

---

[10] We note that in quantities related to the emission process (such as B_ν), ν is short for the rest-frame frequency $\nu_{\rm emit}$, whereas for the observable quantity $S_{\nu,\,\rm obs}$ – the redshifted flux density in the observer's frame – ν implicitly stands for the observed frequency, introducing the factor $(1+z)$.

[11] We introduce the parameterisation of C to relate the true area of dust emission $A^*_{\rm dust}$ (which can only be measured with infinitely high resolution) to its galaxy-averaged value, $A_{\rm dust}$, via $\Sigma_{\rm dust} = M_{\rm dust}/A^*_{\rm dust} = C\,M_{\rm dust}/A_{\rm dust}$, such that $1/C$ represents the covering fraction of dust (we note $C \geq 1$ since $\Sigma_{\rm dust} \geq M_{\rm dust}/A_{\rm dust}$). Unless mentioned otherwise, we assumed $C = 1$ throughout as would be expected for a homogeneous distribution, although a clustered dust distribution (on scales below the resolution of interferometric observations), resulting in $C > 1$, may be more realistic (see Section 4.3).

imation does not hold (Cortzen et al. 2020; Jones et al. 2020a).[12] For a fixed λ_0, an a posteriori consistency check on the assumed opacity model can be performed, since it follows from equations (4) to (6) that

$$\lambda_0 = \left(\kappa_{\nu,\,\mathrm{ref}}\, \Sigma_{\mathrm{dust}}\right)^{1/\beta_{\mathrm{IR}}} \lambda_{\mathrm{ref}}. \tag{8}$$

Alternatively, equation (8) allows for a self-consistent framework around the general greybody SED model in equation (3) where, given a dust mass, we infer λ_0 a priori, which we took as our fiducial opacity model.

Under a set opacity model, we then used a freely varying dust temperature and logarithmic dust mass. As the number of free parameters should not exceed the number of constraints and different assumptions of λ_0 typically dominate over those of the dust emissivity (Casey et al. 2014), we – conservatively, as will become clear in Section 4.3 – fixed the dust emissivity to $\beta_{\mathrm{IR}} = 1.5$. A flat prior within the range $10^4\,\mathrm{M}_\odot < M_{\mathrm{dust}} < M_*$ was assumed on $\log_{10} M_{\mathrm{dust}}$; a gamma distribution with shape parameter $a = 1.5$ and shifted to start at $T_{\mathrm{CMB}}(z)$ was used for the dust temperature (a standard choice for a parameter with a non-negative continuous domain as it is the conjugate prior to many likelihood distributions; we note that there is little difference when assuming a flat prior, but a maximum temperature has to be assumed). The model's predicted observed flux density at a given wavelength are compared with the actual observed flux densities and a likelihood is assigned based on the squared residuals between model and observations (weighted by the inverse variance). Following the formalism in Sawicki (2012), if the model greybody curve exceeds (falls below) the upper limits, the likelihood is lowered (increased) according to the significance of the discrepancy (agreement).

The full SEDs of four galaxies considered in this work are shown in Figure 3. We show one of the two sources for which only upper limits on the dust continuum are available (COS-2987030247), where a range of dust temperatures ($30\,\mathrm{K} \leq T_{\mathrm{dust}} \leq 100\,\mathrm{K}$) and emissivity parameters ($1.5 \leq \beta_{\mathrm{IR}} \leq 2$) for templates that fit the constraints are considered instead of a MERCURIUS fit (idem for UVISTA-Z-007 not shown here). These templates are created under an entirely optically thin opacity model (i.e. an SED described by equation (7)), which is a valid assumption since their dust masses are too small to be confidently detected (as shown in Table 3). As can be seen from these templates, the constraints cannot be used to deduce the best-fit parameters, which is why we report (an upper limit on) the (F)IR luminosity and other parameters with a fiducial temperature $T_{\mathrm{dust}} = 50\,\mathrm{K}$ and $\beta_{\mathrm{IR}} = 1.5$ (Section 3.1). From Figure 3, it can furthermore be seen that the IR luminosity can vary by more than an order of magnitude between the most extreme choices of T_{dust} and β_{IR} (see also Hodge & da Cunha 2020). As described in Section 3.1, we take the systematic uncertainty resulting from fixing these parameters into account in our estimates of the (F)IR luminosity and obscured SFR.

For the three sources for which we have at least one 5σ detection (COS-3018555981, UVISTA-Z-001, and UVISTA-Z-019), on the other hand, the MERCURIUS fitting routine described above is applied, fixing $\beta_{\mathrm{IR}} = 1.5$ but considering different assumptions on the opacity model: either an entirely optically thin SED or the general opacity model, with λ_0 set self-consistently or fixed to an extreme 200 µm. The "best-fit" line shows the SED curve for the maximum likelihood in the $(M_{\mathrm{dust}}, T_{\mathrm{dust}})$ plane, shaded regions show the deviation of the 16th and 84th percentiles from the median (i.e. 50th percentile) at each wavelength of all curves produced according to the posterior distribution. We note the best-fit model of COS-3018555981 and UVISTA-Z-019 is expected not to pass through the $\lambda_{\mathrm{emit}} \sim 160\,\mu\mathrm{m}$ detection, since the upper limit at $\sim 90\,\mu\mathrm{m}$ is also taken into account. In the next two sections, we will discuss the inferred dust properties in more detail.[13]

4.2 The build-up of dust: masses and yields

First, we briefly discuss the estimates of the dust mass of our sources, while stressing these are fairly uncertain, firstly due to the range of possible κ_ν depending on the dust composition as discussed in Section 4.1. Secondly, our measurements do not probe the Rayleigh-Jeans (RJ) tail of the SED, meaning that the dust mass becomes sensitive on the intrinsic dust temperature: sampling at a rest-frame wavelength 200 µm introduces a factor ~5 difference in M_{dust} for a 2× difference in T_{dust}, for instance (Cortzen et al. 2020). The latter effect, however, is reflected in the uncertainty estimates from the posterior distributions obtained in the MERCURIUS fitting routine, which probes a range of temperatures. As will be discussed below, the distributions are based purely on the likelihood of underlying dust masses and temperatures producing the observed continuum (non-)detections and in principle could result in unphysical scenarios (save dust masses above the stellar mass and temperatures below the CMB temperature, whose solutions are discarded; Section 4.1).

For the five sources considered in this work, we find the dust mass typically range upwards of a few million solar masses. Interestingly, the tentatively low dust temperature of COS-3018555981 (discussed in more detail in Section 4.3) under the fiducial self-consistent general opacity model (where $\lambda_0 \simeq 10\,\mu\mathrm{m}$) nominally implies a relatively high dust mass, $M_{\mathrm{dust}} = 7^{+19}_{-5} \cdot 10^7\,\mathrm{M}_\odot$. Since the self-consistently derived λ_0 is well below the lowest sampled wavelength ($\lambda_{\mathrm{emit}} \sim 90\,\mu\mathrm{m}$), an optically thin SED appears a rather good approximation producing a similar dust mass and temperature, although the estimated uncertainty in the self-consistent model is larger and thus more conservative (mainly allowing for even higher dust masses that are compensated for by an increasing λ_0).

The estimated dust mass translates into a substantial dust-to-stellar mass ratio, $M_{\mathrm{dust}}/M_* = 0.05^{+0.16}_{-0.04}$ (Table 3). Although we stress the current evidence is limited, the formal likelihood treatment evidently yields rather extreme solutions; might we expect the true values be more modest from a physical perspective? We consider dust grains comprise of metals mainly produced by short-lived, massive stars, while most of the stellar mass instead is dominated by low-mass stars, so that M_{dust}/M_* cannot exceed the stellar metallicity yield – the mass-fraction of metals released into the ISM compared to the total (remaining) stellar mass – typically assumed to be a few percent (Maiolino & Mannucci 2019). However, higher stellar yields are certainly plausible for a (more) top-heavy IMF: for instance, a Kroupa (2001) or Chabrier (2003) IMF already results in stellar metallicity yields that are twice as high than for a Salpeter (1955) IMF (Vincenzo et al. 2016). Moreover, we note the stellar mass estimate of $M_* = 1.4^{+0.7}_{-0.2} \cdot 10^9\,\mathrm{M}_\odot$ (taken from Smit et al. 2018) is a conservative one in this context as it is ~0.5 dex

---

[12] Together with the fact that the intrinsic dust temperature has a large impact on the derived dust masses at shorter wavelengths, this is why dust masses should ideally be inferred from the highest FIR wavelengths ($\lambda_{\mathrm{emit}} > 450\,\mu\mathrm{m}$), where the SED certainly is optically thin (Casey 2012).

[13] Unless mentioned otherwise, reported quantities are given as the 50th (i.e. median), 16th, and 84th percentiles (as a $\pm 1\sigma$ confidence range) of the parameter's marginalised posterior distribution.

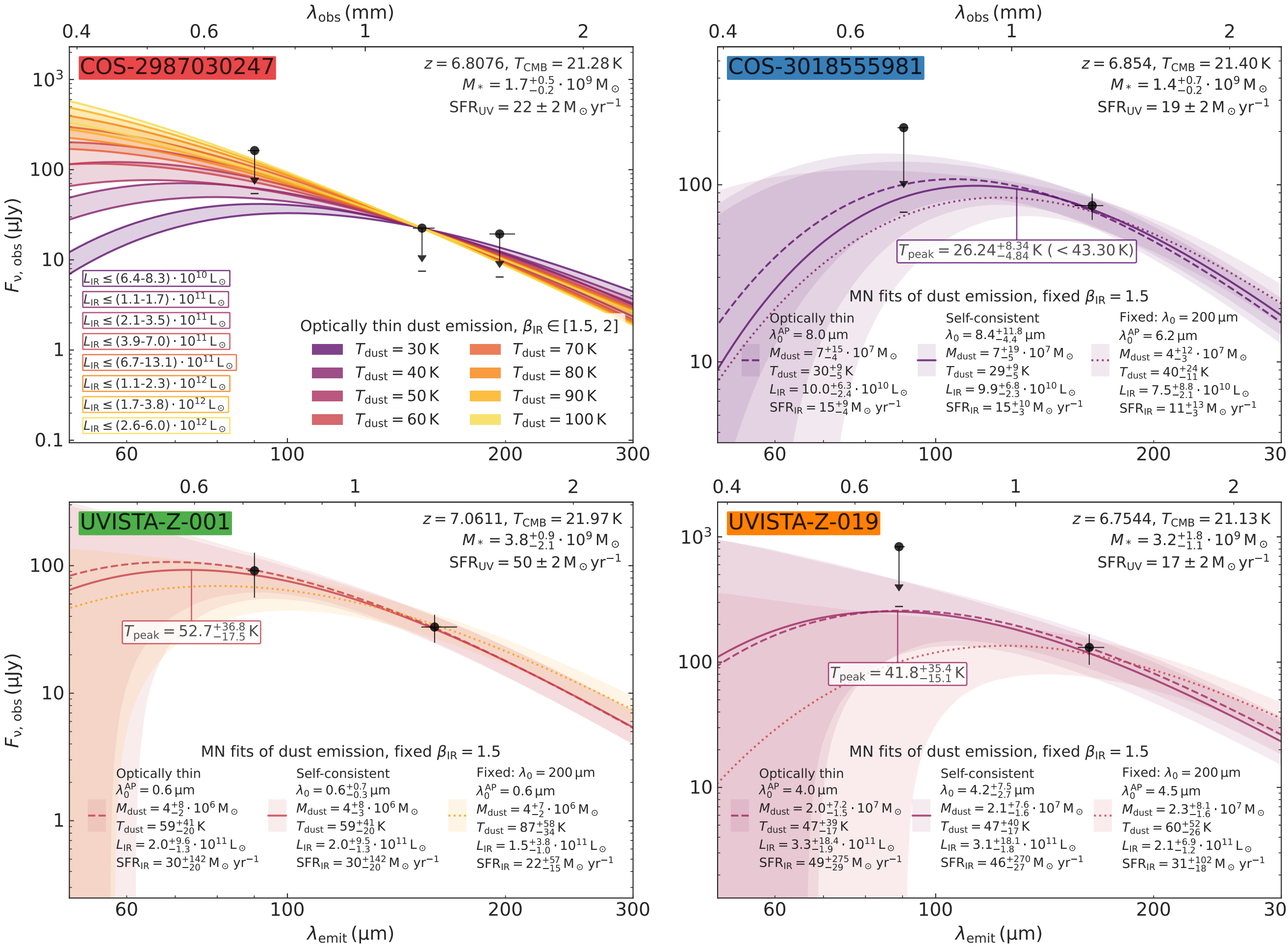

Figure 3. Overview of the dust continuum detections and upper limits for four galaxies investigated in this work. Upper limits are drawn at 3σ, with a line beneath indicating a 1σ level. Where only upper limits are available (i.e. for COS-2987030247), we plot a wide variety of greybody dust SEDs, for $30\,{\rm K} \leq T_{\rm dust} \leq 100\,{\rm K}$ and $1.5 \leq \beta_{\rm IR} \leq 2$ (under an entirely optically thin opacity model). The resulting range of IR luminosities is indicated in the bottom left, showing $L_{\rm IR}$ can vary by more than an order of magnitude between the most extreme choices of $T_{\rm dust}$ and $\beta_{\rm IR}$. For COS-3018555981, UVISTA-Z-001, and UVISTA-Z-019, on the other hand, the MERCURIUS fitting routine described in Section 4.1 is applied, fixing $\beta_{\rm IR} = 1.5$ but considering various assumptions on the opacity model: either an entirely optically thin SED or the general opacity model given in equation (6) with either a self-consistent or fixed λ_0, the wavelength separating the optically thick and thin regimes. The "best-fit" line shows the SED curve for the maximum likelihood in the $(M_{\rm dust}, T_{\rm dust})$ plane, shaded regions show the 16th and 84th percentiles at each wavelength of all curves produced according to the posterior distribution. We note the best-fit model of COS-3018555981 and UVISTA-Z-019 is expected not to pass through the $\lambda_{\rm emit} \sim 160\,\mu$m detection, since the upper limit at $\sim 90\,\mu$m is also taken into account. The resulting dust mass and temperature are indicated for each fit, as is $\lambda_0^{\rm AP}$, the value of λ_0 that is inferred a posteriori (if applicable). The inferred peak temperature (though measured on the CMB-corrected spectrum; Appendix A) for the fiducial self-consistent opacity model is annotated (see also Table 3).

higher than the best fit found by the REBELS collaboration, who explored several photometric fitting codes (private communication, REBELS collaboration 2021; see also Bouwens et al. 2022). Upcoming *James Webb Space Telescope* (*JWST*) observations (GTO: 1217, GO: 1837) will provide a highly accurate stellar mass and give insight into the star formation history of this source, and hence also its age.

By assuming a stellar IMF, the dust-to-stellar mass ratio can be converted into a dust yield, denoted $y_{\rm dust}$, which represents the average dust mass formed per dust-producing star. Here, we follow the method of Michałowski (2015), who considered SNe and asymptotic giant branch (AGB) stars as sources of dust production, assuming their relevant stellar mass ranges are 8-40 $\rm M_\odot$ and 3-8 $\rm M_\odot$, respectively. Both yields from SNe and AGB stars for a Chabrier (2003) IMF are shown in Table 3. Average AGB dust yields that are obtained under Salpeter and top-heavy IMFs can be $\sim 2\times$ higher, but this only strengthens the interpretation discussed below. More critically, however, the inferred SN dust yields could decrease (increase) by a factor of ~ 1.5 for a top-heavy (Salpeter) IMF since these IMFs result in a higher (lower) number of SN events, thereby lowering (raising) the required average yield per SN.

The yield that would be required per AGB star, $y_{\rm dust,\,AGB} \sim 1.5^{+4.6}_{-1.1}\,\rm M_\odot$ for COS-3018555981, far exceeds the theoretically expected value, $\sim 0.02\,\rm M_\odot$, even more so when the yield is increased up to $2\times$ under a different IMF (as already shown for other EoR galaxies in e.g. Michałowski 2015; Leśniewska & Michałowski 2019; Schouws et al. 2022b). This renders AGB stars an unlikely candidate as the main source of dust formation in this early cosmic epoch (even within the systematic uncertainty of $\kappa_{\nu,\,\rm ref}$). Instead, when SNe are considered, a nominally gigantic yield of $y_{\rm dust,\,SN} = 4.5^{+13.3}_{-3.1}\,{\rm M}_\odot$ per dust-producing star would be required. We note that the uncertainty estimates, apart from incorporating a systematic 10% flux calibration uncertainty (Section 3.1), are purely statistical and the SN dust yield could systematically be reduced by a high $\kappa_{\nu,\,\rm ref}$ resulting in a lower dust mass (see Section 4.1). However, as also discussed in Section 4.1, the current assumption of $\kappa_{\nu,\,\rm ref} = 8.94\,{\rm cm^2\,g^{-1}}$ is valid for dust produced by SNe and thus other choices would be inconsistent for estimating the SN dust yield.

Even the lowest required yield within the estimated 1σ uncertainties, $\sim 1.4\,{\rm M}_\odot$, is already in slight tension with the maximum theoretical yield per SN, which is 1 to $2\,{\rm M}_\odot$ without the subsequent dust destruction by the SN (e.g. Nozawa et al. 2003). The discrepancy might even be more serious for various reasons: if dust destruction does play a significant role, this lowers the theoretical maximum yield, while the required dust yield per SN is increased under a different IMF. Finally, we find yet a lower dust temperature and higher mass and yield increase if we instead assume a higher dust emissivity $1.8 \lesssim \beta_{\rm IR} \lesssim 2$, the value typically found at high redshift for more massive systems (e.g. Jones et al. 2020a; Cortzen et al. 2020; Faisst et al. 2020; Casey et al. 2021) – this is why we conservatively opt for a fiducial $\beta_{\rm IR} = 1.5$ here. Hence, there is tentative evidence that other evolutionary mechanisms, such as the growth of dust grains in the ISM (Leśniewska & Michałowski 2019), need to be invoked. A final caveat to this result is that the dust mass decreases if λ_0 is fixed to 200 µm (since higher temperatures are feasible in this scenario; Section 4.3), thereby bringing the dust yield down to $y_{\rm dust,\,SN} \sim 3\,{\rm M}_\odot$, which however is still inconsistent with theoretical expectations. Yet this scenario would perhaps be equally surprising, as will be discussed further in Section 4.3.

4.3 Cosmic evolution of dust temperature: evidence for extremely cold or highly clustered dust?

In the following, we move on to discuss the dust temperature, arguably one of its most important properties as it is essential in deriving other observable quantities such as the infrared luminosity and dust mass from a limited number of photometric data points (Sommovigo et al. 2020, 2022). Unfortunately, establishing the dust temperature is not trivial. Directly fitting observed SEDs necessarily yields a luminosity-weighted dust temperature, which may be skewed towards high temperatures by hot dust in star-forming regions (Liang et al. 2019). Hot dust can only be observed directly, however, if the emission is optically thin (Faisst et al. 2020). When little information is available, these effects cause the dust temperature, mass, and opacity to become degenerate.

In Figure 4, measurements of the SED peak temperature across cosmic time are shown. The peak temperature is defined as a purely observational quantity, defined similarly to Wien's displacement law using the SED peak wavelength[14] in the rest frame, $\lambda_{\rm emit,\,peak}$:

$$T_{\rm peak} = \frac{b}{\lambda_{\rm emit,\,peak}},\ \text{where } b \simeq 2898\,{\rm K/\mu m}. \tag{9}$$

Details on the motivation for comparing peak temperatures, rather than $T_{\rm dust}$, and the precise data from the literature that is included can be found in Appendix A. We report "intrinsic" peak temperatures, in the sense that there is no conversion to the current epoch ($z = 0$) to nullify the effect of CMB heating at the relevant epoch, for two reasons. Firstly, peak temperatures are an observational construct (lower than the intrinsic dust temperature), and secondly, in most cases, the dust has already largely decoupled from the CMB and heating (described by equation (12) of da Cunha et al. 2013) starts to become relevant only when going back in cosmic time significantly or for extremely cold dust that has cooled down nearly to the CMB temperature. This is illustrated by the red shaded region, which marks an increase of more than 1% in dust temperature between $z = 0$ and the relevant redshift (under $\beta_{\rm IR} = 1.5$) and falls below almost all measurements shown here (although neglected in Figure 4, we will apply this correction when relevant in the following).

Although a consistent picture starts to emerge at $z \lesssim 4$ (e.g. Schreiber et al. 2018; Drew & Casey 2022), it is unclear whether this also applies to galaxies in the EoR due to limited observational data and the highly uncertain relative importance of the possible mechanisms of dust formation (Mancini et al. 2015). Theoretical models predict elevated dust temperatures compared to the local Universe (e.g. Ma et al. 2019; Sommovigo et al. 2020; Vijayan et al. 2022), which is indeed confirmed by observations in some cases (with extreme examples given in Behrens et al. 2018; Bakx et al. 2020; Viero et al. 2022). However, the peak temperatures for several objects – most notably $T_{\rm peak} \sim 28$ K seen in J0217-0208 (Harikane et al. 2020) – are lower than what may be expected from an extrapolation of the trend at low redshift (such as the shown fit by Schreiber et al. 2018; see also Bouwens et al. 2020) and theoretical predictions from cosmological hydrodynamic simulations (e.g. Liang et al. 2019; Vijayan et al. 2022). As pointed out by Sommovigo et al. (2022), a large scatter in dust temperatures may be expected at early times owing to strongly varying physical conditions in the complex high-redshift ISM. This encourages detailed follow-up studies of objects with seemingly extreme dust properties such as COS-3018555981, as we will discuss in the following.

We place a constraint on the peak temperature through the MERCURIUS fitting procedure for COS-3018555981, UVISTA-Z-001, and UVISTA-Z-019, the three sources for which we have at least one confident detection. However, despite a $\sim 7\sigma$ detection at ~ 160 µm (Figure 1), the upper limit at $\lambda_{\rm emit} \sim 90$ µm is not stringent enough to provide precise constraints on the dust temperature of UVISTA-Z-019. Therefore, we show its median value and 68% confidence range in Figure 4 for the fiducial opacity model with self-consistent λ_0 (as listed in Table 3). While this result does not change significantly under a different opacity model, the estimated uncertainty is so high that within 1σ deviations, it is consistent with strongly varying scenarios, confirming the temperature is largely unconstrained. With two detections, we estimate the dust temperature in UVISTA-Z-001 to be $T_{\rm dust} = 59^{+41}_{-20}$ K. However, due to the matched apertures we have chosen (see Section 3.1), we note this temperature is representative for the compact component only; the data at ~ 160 µm reveals an extended dust-continuum emission that is not detected at ~ 90 µm, suggesting a colder dust reservoir exists on larger scales (see also Akins et al. 2022).

Similarly, the dust-continuum measurements of COS-3018555981 – a deep ~ 90 µm non-detection combined with a significant ~ 160 µm detection – favour a low dust temperature for this object. In the fiducial self-consistent opacity model (where we find $\lambda_0 \simeq 10$ µm, i.e. effectively almost optically thin), we even find a nominal intrinsic temperature of $T_{\rm dust} = 29^{+9}_{-5}$ K or alternatively, an upper limit of $T_{\rm dust} < 48$ K (95% confidence). The median estimate

---

[14] The peak of the intrinsic SED, i.e. after it has been corrected for observing the dust emission against the CMB (Section 4.1).

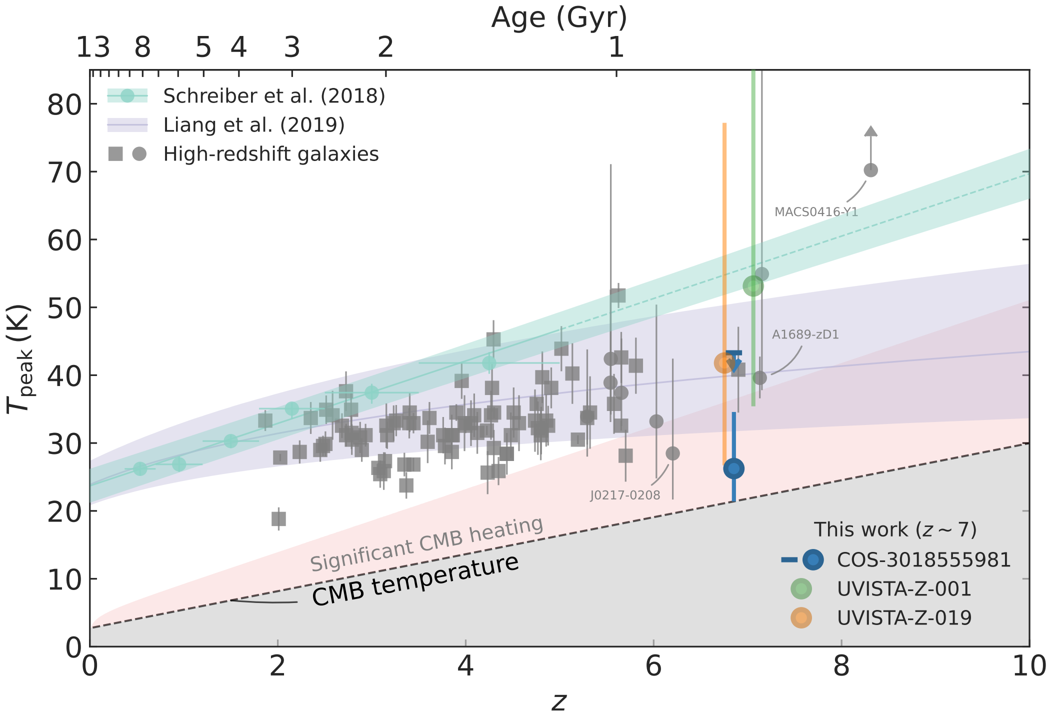

Figure 4. Dust peak temperature, $T_{\rm peak}$, as a function of cosmic time. Several peak temperatures derived from measurements presented in this work under the self-consistent general opacity model are drawn: for UVISTA-Z-019, we show its median and 68% confidence range (largely invariant under the chosen opacity model), while for COS-3018555981 an upper limit (95% confidence) is shown in addition. Further, measurements inferred from stacked spectra and a (partially extrapolated) linear fit by Schreiber et al. (2018) are shown, as is the power-law fit to the peak-temperature evolution of simulated galaxies by Liang et al. (2019). Details on the literature data points can be found in Appendix A (SMGs are shown as squares, other high-redshift galaxies as circles with errorbars). Three sources are highlighted with labels, having either a notably low (J0217-0208), high (MACS0416-Y1), or accurately constrained dust temperature (A1689-zD1). The grey dashed line shows the CMB temperature over cosmic time, the grey area below representing astrophysically unattainable temperatures – we note, however, that effective peak temperatures of greybody SEDs can in principle fall below this boundary as they are lower than the dust temperature itself (Section 4.3). The light-red area above indicates the region where CMB heating has a significant (greater than 1%) effect compared to $z = 0$ (see Section 4.3 for details).

begins to approach ~ 21 K, the CMB temperature at $z \sim 7$.[15] As noted in Section 4.2, the temperature becomes even lower (likewise, the dust mass and dust yield increase) if we instead assume a higher dust emissivity such as $\beta_{\rm IR} = 2$, which effectively causes the optical depth to drop more quickly towards higher wavelengths. The peak temperature is $T_{\rm peak} = 26^{+8}_{-5}$ K, shown in Figure 4 as the blue circle along with an upper limit: $T_{\rm peak} < 43$ K (95% confidence). Such low temperatures are at odds with $T_{\rm peak}$ measurements of other galaxies at $z \sim 7$ – with the notable exception of J0217-0208 (Harikane et al. 2020) – as well as with theoretical predictions (e.g. Liang et al. 2019) and extrapolated observed behaviour at low redshift (Schreiber et al. 2018) of the peak-temperature evolution.

In the general opacity case, though, the likelihood of higher peak temperature increases since greybody SED templates can, if they are sufficiently optically thick, become possible within the constraints even when their peak wavelength would otherwise fall below 90 μm (i.e. $T_{\rm peak} \gtrsim 32$ K). When $\lambda_0 = 200$ μm, the upper limit relaxes slightly to $T_{\rm peak} < 53$ K (though the median and 1σ confidence ranges are mostly unaffected, as expected when comparing the peak temperature; see Appendix A for details). Moreover, this optically thick scenario favours a fit with a significantly higher intrinsic temperature of $T_{\rm dust} = 40^{+24}_{-11}$ K, albeit somewhat uncertain since a larger range of temperatures is now allowed.

At first glance, an SED that only turns optically thin at ~ 200 μm seems to alleviate the tentative tension of an extremely low dust temperature (and high dust mass and yield, cf. Section 4.2). This in itself is a surprising finding, though, since such a high λ_0 is typically seen in ULIRGs or even HyLIRGs (e.g. Faisst et al. 2020; Cortzen et al. 2020). LIRGs (luminous infrared galaxies) are a class of galaxies defined by IR luminosity exceeding $10^{11}\,{\rm L}_\odot$ (and would therefore include UVISTA-Z-019 and within the uncertainty, possibly even the other three sources; Table 3). The ultra- and hyper-variants, ULIRGs and HyLIRGs, exhibit an $L_{\rm IR}$ of more than $10^{12}\,{\rm L}_\odot$ and $10^{13}\,{\rm L}_\odot$, respectively (Sanders & Mirabel 1996); such extreme systems commonly have dust reservoirs of $10^8\,{\rm M}_\odot$ or even larger and contain very compact star-forming regions accompanied by high surface densities of SFR, gas, and dust (Clements et al. 2010).

Indeed, we find a comparatively low dust surface mass density of a few ${\rm M}_\odot\,{\rm pc}^{-2}$ (Table 3). To put this in perspective, this is two orders of magnitude lower than $\sim 500\,{\rm M}_\odot\,{\rm pc}^{-2}$ found for a massive HyLIRG starburst at $z \sim 4$ for which $\lambda_0 = 170 \pm 23$ μm (Cortzen et al. 2020). Hence, the resulting a-posteriori estimates for λ_0 in an opacity model with fixed $\lambda_0 = 200$ μm are more than an order of magnitude lower than what is assumed ($\lambda_0^{\rm AP} \sim 5$ μm; see Figure 3). This discrepancy would point towards the need of a highly

---

[15] The lower end of the 68% confidence range actually enters the regime where CMB heating plays a significant role such that $T_{\rm dust}^{z=0} = 28^{+10}_{-7}$ K when translated to $z = 0$.

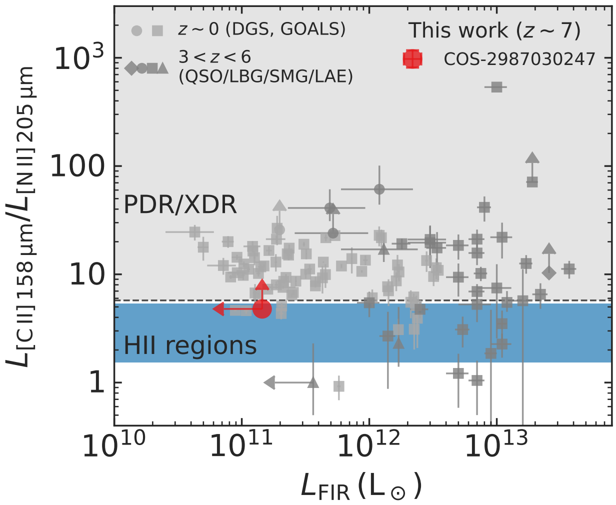

Figure 5. Luminosity ratio of [C II] 158 μm over [N II] 205 μm as a function of the FIR luminosity. Local galaxies shown are from GOALS (Díaz-Santos et al. 2017) and DGS (Cormier et al. 2015, 2019); constraints on high-redshift galaxies (Decarli et al. 2014; Pavesi et al. 2016, 2019) and SMGs as part of the SPT survey (Cunningham et al. 2020) are included as well (see Section 5.1 for details). LBGs are indicated with circles, SMGs with squares, LAEs with upward facing triangles, and the quasar (QSO) as a diamond. The luminosity ratio expected for [C II] emission originating in H II regions for typical physical conditions (solar metallicity and $\log_{10} U < -3$, $n_{\mathrm{H}} < 10^2\,\mathrm{cm}^{-3}$; see Section 5.1) is shown as the blue shaded area. A dashed line demarcates $L_{[\mathrm{C\,II}]}/L_{[\mathrm{N\,II}]} \simeq 6$, the minimum value found across a large range of PDR models (grey shaded area; a similar neutral medium can be created in the presence of X-ray dominated regions (XDRs) or shocked gas, see e.g. Decarli et al. 2014). For COS-2987030247, the 3σ upper limit on [N II] is fully consistent with [C II] production in a PDR-like medium.

clustered distribution of dust in order to produce a self-consistent optical depth: from equations (4) and (8), this would require $C \gg 1$ ($C \sim 10^3$ to increase λ_0^{AP} by a factor of 100, for $\beta_{\mathrm{IR}} = 1.5$).

In conclusion, the results lead to a paradox with a remarkably low dust temperature in combination with high dust mass and yield on the one hand (optically thin SED), or the need of a highly clustered dust distribution (optically thick SED) on the other. In either case, follow-up observations are needed to clarify the tantalising dust properties of COS-3018555981.

5 EMISSION LINE PROPERTIES

5.1 On the origin of [N II] 205 μm and [C II] 158 μm emission

The line ratio of [C II] to [N II] is a well-known probe of the ionisation state of the ISM (e.g. Nagao et al. 2012). The [N II] 205 μm transition namely has a critical density very close to that of [C II] 158 μm ($\sim 50\,\mathrm{cm}^{-3}$ in ionised gas; e.g. Carilli & Walter 2013), while the ionisation potentials of C^+ (24.4 eV) and N^+ (29.6 eV) are also comparable (e.g. Decarli et al. 2014). In addition, the ionisation potential of neutral carbon (11.3 eV) and nitrogen (14.5 eV) are similar, but crucially just below and above that of hydrogen (13.6 eV). Therefore, while [N II] strictly originates in regions where hydrogen is (largely) ionised, [C II] emission can arise in both H II regions and PDRs. For this reason, the line ratio of [C II] to [N II] is a powerful proxy of the ionisation state of the [C II]-producing gas, independent of, for example, the ionisation parameter (e.g. Nagao et al. 2012).

Table 5. Molecular gas masses, M_{mol}, estimated from the [C II] 158 μm luminosity (Table 4) using the conversion given in Zanella et al. (2018). Also given are $M_{\mathrm{mol}}/M_{\mathrm{dust}}$ and M_{mol}/M_*, (lower limits of) the gas-to-dust and gas-to-stellar mass ratios (see Section 5.1 for details).

Source	M_{mol} ($10^9\,\mathrm{M}_\odot$)	$M_{\mathrm{mol}}/M_{\mathrm{dust}}$	M_{mol}/M_*
COS-2987030247	8.8 ± 4.8	$\gtrsim 2.5 \cdot 10^3$	$5.2^{+2.9}_{-3.1}$
COS-3018555981	12.3 ± 2.2	$1.7^{+3.7}_{-1.3} \cdot 10^2$	$8.9^{+2.2}_{-3.4}$
UVISTA-Z-001	20.9 ± 7.9	$5.8^{+13.3}_{-4.5} \cdot 10^3$	$5.5^{+7.1}_{-2.3}$
UVISTA-Z-007	14.2 ± 5.0	$\gtrsim 1.2 \cdot 10^3$	$3.8^{+6.8}_{-2.5}$
UVISTA-Z-019	23.8 ± 3.8	$1.2^{+4.5}_{-0.9} \cdot 10^3$	$7.4^{+4.0}_{-2.9}$

In Figure 5, we compare the [C II]/[N II] ratio of COS-2987030247 (lower limit of $L_{[\mathrm{C\,II}]}/L_{[\mathrm{N\,II}]} > 4.8$ at 3σ, see Section 3.2) against a number of sources from the literature, as a function of the FIR luminosity.

In this figure, several local galaxies are shown, all observed by *Herschel*/PACS: local (U)LIRGs from the GOALS survey (Díaz-Santos et al. 2017), as well as one lower limit that is part of the Dwarf Galaxy Survey (DGS; Cormier et al. 2015, 2019); both surveys will be discussed in more detail in Section 5.2. Furthermore, a sample of $3 \lesssim z \lesssim 6$ SMGs observed by the SPT is shown (Cunningham et al. 2020; FIR luminosities are presented in Reuter et al. 2020). We also include several individual high-redshift sources: a quasar (QSO), SMG, and two Lyα emitting galaxies (LAEs) presented in Decarli et al. (2014), and several LBGs from Pavesi et al. (2016, 2019).

While Decarli et al. (2014) report the typical luminosity ratio expected for [C II] emission originating in H II regions to be $L_{[\mathrm{C\,II}]}/L_{[\mathrm{N\,II}]} \sim 2$, we indicate here the range of line ratios found across a large range of photoionisation models, which will be introduced in Section 5.3. We show the luminosity ratio expected for pure H II regions with typical gas conditions (solar metallicity and $\log_{10} U < -3$, $n_{\mathrm{H}} < 10^2\,\mathrm{cm}^{-3}$), but we note the ratio can increase with a lower metallicity, higher ionisation parameter, and/or higher gas density (in addition to a sub-solar C/N ratio). The line ratios predicted for models incorporating a PDR (see Section 5.3 for details) can be substantially higher, suggesting the line ratios of the majority of the observations are consistent with an additional component of [C II] being produced in a neutral PDRs environment (or similarly in X-ray dominated regions (XDRs) or shocked gas; Decarli et al. 2014, and references therein). For COS-2987030247, the 3σ upper limit on [N II] is fully consistent with [C II] production in a PDR-like medium. While it does simultaneously allow for H II regions as the primary origin of the [C II] emission, the upper limit suggests this scenario is unlikely (for reasonable physical conditions) at a $\sim 2\sigma$ level.

Having established that a contribution to the [C II] 158 μm emission of COS-2987030247 is likely traced to a neutral, PDR-like medium, we expect the same to be true for the other three $z \sim 7$ star-forming galaxies with similar physical properties. Indeed, this is in line with recent findings of high H I gas mass fractions at early times (Heintz et al. 2021, 2022). Moreover, Zanella et al. (2018) have showed there exists a linear relation between the [C II] luminosity and the molecular gas mass of a galaxy, regardless of its gas depletion time (i.e. starburst or main-sequence phase), redshift, and metallicity. Since all galaxies have confident [C II] detections, we can easily convert $L_{[\mathrm{C\,II}]}$ into an estimate of M_{mol}, the molecular gas mass, though we caution our sources are beyond the redshift (and possibly metallicity) regime at which Zanella et al. established the calibration. We adopted their median conversion factor of $\alpha_{[\mathrm{C\,II}]} = 31\,\mathrm{M_\odot\,L_\odot^{-1}}$ and a systematic 0.3 dex spread. The results are shown in Table 5. We also provide estimates on the gas-to-dust and gas-to-stellar mass ratios, which, in the form of $M_{\mathrm{mol}}/M_{\mathrm{dust}}$ and M_{mol}/M_* respectively, are strictly lower limits since we do not take into account the H I gas mass. Interestingly, we find a modest gas-to-dust ratio for COS-3018555981 (albeit a lower limit), which implies a high metallicity (Rémy-Ruyer et al. 2014). We note this would be consistent with the findings in Section 4.2 requiring a high metal yield.

We now turn to a discussion focused on the [O III] 88 μm line in comparison to [C II] 158 μm and in the context of the optical [O III] lines (inferred from *Spitzer* broadband photometry so that these include [O III] $\lambda\lambda$ 4960, 5008 Å and Hβ; see Section 2.1).

5.2 [O III] 88 μm and [C II] 158 μm in the local and high-redshift Universe

In the local Universe, two main samples of galaxies with measurements of several FIR lines (including [O III] and [C II]) exist, as mentioned in Section 5.1: firstly, GOALS has observed over 200 (U)LIRGs at $z \sim 0$ with *Herschel*/PACS and *Herschel*/SPIRE (Díaz-Santos et al. 2017); secondly, the DGS uses *Herschel*/PACS to investigate just under 50 metal-poor dwarf galaxies (Madden et al. 2013, 2014; De Looze et al. 2014; Cormier et al. 2015, 2019). Among the dwarf galaxies of the DGS, the luminosity ratio of [O III] 88 μm to [C II] 158 μm varies between 0.5 and 13 with a median of 2, whereas the median ratio for 159 of the (U)LIRGs where both lines are detected is an order of magnitude smaller (namely ~ 0.2, varying between 0.04 and 3). Cormier et al. (2015) argue that a large filling factor of diffuse, ionised gas emitting [O III] 88 μm is needed to explain the observed ratios in dwarf galaxies. Crucially, metal-poor systems may therefore have a more porous ISM through which ionising radiation could escape, which implies that the [O III]/[C II] ratio can indicate leakage of Lyman-continuum (LyC) radiation (see also Inoue et al. 2016; Katz et al. 2020).

Similar to the metal-poor dwarf galaxies, star-forming galaxies in the EoR have been shown to exhibit systematically high [O III]/[C II] ratios between 1 and 10 (Harikane et al. 2020), which is confirmed by our findings of (integrated) line ratios between around 2 and 8 (Table 4). Given the limited amount of significant detections and ancillary observations, however, it is not straightforward to disentangle the contributions of various physical properties that influence the observed ratios of galaxies in the early Universe. First of all, there may be certain observational systematics or selection biases. For instance, flux measurements in interferometric data sets have to be treated carefully, since the spatial extent of the [C II] emission has been shown to be significantly larger than that of [O III] (Carniani et al. 2018a, 2020; see also Section 2.2.2). Even when accounting for the extended [C II] emission, various studies have suggested that the typical EoR galaxy has even higher [O III]/[C II] ratios than found even in local metal-poor dwarf galaxies (Carniani et al. 2020; Harikane et al. 2020). High [O III]/[C II] ratios are generally indicative of strong bursts of star formation with short gas depletion times ($t_{\mathrm{dep}} \lesssim 50$ Myr; Vallini et al. 2021), which may be common among the UV-bright galaxies at high redshift that have typically been selected for follow-up spectroscopy with ALMA.

The specific star formation rate (sSFR) is expected to scale inversely with the age of the stellar population in a galaxy, implying that such strong, recent bursts of star formation should be indicated by a high sSFR (Vallini et al. 2021). Indeed, galaxies at high redshift ($z \gtrsim 6$) that have been observed in both [O III] 88 μm and [C II] 158 μm (see e.g. Carniani et al. 2020) are characterised by higher sSFRs (roughly 1 to 2 dex) than galaxies from the local DGS and GOALS samples. However, the DGS and GOALS samples share a similar median sSFR of 0.31 Gyr^{-1} and 0.36 Gyr^{-1} respectively, despite having a factor of ~ 10 difference in their [O III]/[C II] ratios, making the global sSFR of galaxies a poor indicator of high [O III]/[C II] emission. Potentially, the local dwarf galaxies have a (much) older stellar component (e.g. Mateo 1998), which lowers their global stellar mass and overall sSFR, while merely their young star-forming regions – possibly fuelled by recent inflows of gas –

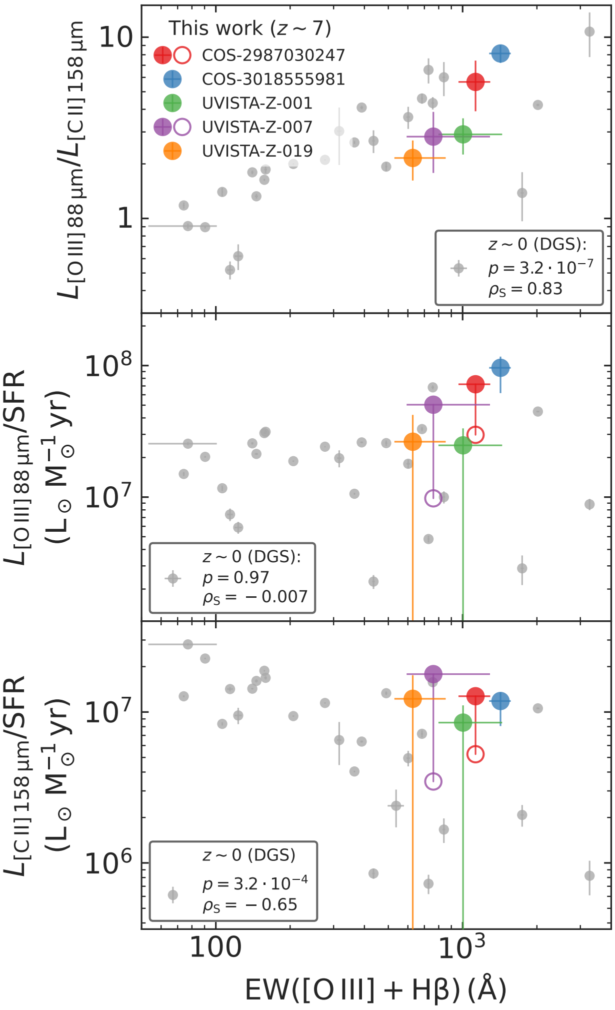

Figure 6. Ratios of the [O III] 88 μm and [C II] 158 μm luminosities with respect to each other (top panel) and with respect to the SFR (middle panel for [O III], bottom panel for [C II]) as a function of the EW of the optical [O III] and Hβ lines. If the measured SFR is an upper limit (due to a non-detection of the dust continuum), unobscured SFR measurements are shown with an open circle. Small grey circles are galaxies from DGS (see Section 5.2). The p-value, for a null hypothesis that the data are uncorrelated, and Spearman's rank correlation coefficient (ρ_S) of these points measured in logarithmic space are indicated in each panel. Coloured circles show the five $z \sim 7$ galaxies considered in this work. There is a significant positive correlation between the [O III]/[C II] ratio and their optical EW among the DGS galaxies, which seems to derive mostly from a negative correlation between [C II]/SFR and the EW; however, the correlation of the [O III]/[C II] luminosity ratio is stronger than that of the (relative) [C II] luminosity on its own. Furthermore, it is unclear whether the same is true for the small sample of high-redshift galaxies.

are thought to have the most similar ISM conditions to high-redshift galaxies. Alternatively, the time scales on which SFRs are measured may be too long to give an accurate indication of their [O III]/[C II] ratio, since most galaxies in DGS and GOALS have SFRs measured through their (UV and) IR luminosity (probing time scales on the order of 100 Myr; e.g. Kennicutt & Evans 2012).

We therefore consider an alternative (inverse) tracer of starburst age, the EW of the optical [O III] and Hβ lines, which makes a fairer comparison between local and distant galaxies specifically when the EW is measured across the young star-forming regions of local dwarf galaxies.[16] In the top panel of Figure 6, we show the [O III]/[C II] luminosity ratio as a function of the EW of the optical [O III] and Hβ lines both for the DGS and $z \sim 7$ galaxies considered in this work.[17] Among the metal-poor dwarf galaxies, there is a clear positive correlation: the Spearman's rank correlation coefficient measured in logarithmic space is $\rho_\mathrm{S} \simeq 0.83$ (with a p-value of $3.2 \cdot 10^{-7}$); this is noticeably higher than when EW is swapped for sSFR, where $\rho_\mathrm{S} \simeq 0.35$ ($p \simeq 0.056$). In the bottom two panels of Figure 6, we investigate whether this effect is mostly due to brighter [O III] 88 μm line or a [C II] 158 μm deficit towards higher EWs (and hence younger ages). The correlation coefficients suggest it derives mostly from a negative correlation between [C II]/SFR and the EW ($\rho_\mathrm{S} \simeq -0.65$ with $p \simeq 3.2 \cdot 10^{-4}$) rather than between [O III]/SFR and EW ($\rho_\mathrm{S} \simeq -0.007$ with $p \simeq 0.97$); however, the correlation of the [O III]/[C II] luminosity ratio is stronger than that of the (relative) [C II] luminosity on its own. Furthermore, it is unclear whether the same is true for the small sample of high-redshift galaxies (where indeed the opposite seems true).

To investigate whether the observed line intensities line up with theoretical expectations, we will introduce a set of photoionisation models aimed to mimic the expected physical condition of the ISM in the following.

5.3 Comparing observed emission line strengths to the predictions of photoionisation models

To gain further insight into the physical conditions of the ISM, we employed one-dimensional, radiative-transfer models of a plane-parallel nebula in CLOUDY (v17.02; Ferland et al. 2017) to simulate an H II region that smoothly transitions into a PDR. As the incident radiation field, we used a single burst of star formation with varying ages generated by BPASS v2.1 (Eldridge et al. 2017) under a Salpeter IMF, ranging in stellar mass from 1 to 100 $\mathrm{M}_\odot$. Motivated by for example the observed extreme optical EWs, we choose the set of BPASS models where interacting binary stars are included (significantly boosting the ionising flux; see e.g. Stanway et al. 2016). In addition, the CMB at $z = 7$ and a cosmic ray background (crucial to the PDR physics; see Abel et al. 2005) are included in all models. Following Cormier et al. (2019), we chose a density law that increases linearly with column density, resulting in an exponential density profile that is nearly constant in the H II region.[18] As in Harikane et al. (2020), we explored stellar metallicities of $Z_*/\mathrm{Z}_\odot \in \{0.05, 0.2, 1\}$ where, as a baseline model, we set the gas metallicity Z_neb equal to that of the stars under the default abundance pattern in CLOUDY (which has $12 + \log{(\mathrm{O/H})}_\odot = 8.69$; Asplund et al. 2009), except for helium which we set according to equation (1) in Groves et al. (2004).

We varied the ionisation parameter between $\log_{10} U = -4$ and -0.5, in steps of 0.5, while fixing the hydrogen density to $n_\mathrm{H} \sim 10^2\ \mathrm{cm}^{-3}$ (both defined at the illuminated face of the cloud). Though we do explore different gas densities (as discussed below), the choice for this particular value was motivated both by observations at high redshift (e.g. Sanders et al. 2016) and typical densities found in local dwarf galaxies that show similarly strong [O III] 88 μm emission relative to their SFR, such as Mrk 209 (Izotov et al. 1997) and II Zw 40 (Guseva et al. 2000). Graphite and silicate dust grains with Orion-like size distribution and abundance were included, along with a self-consistent abundance correction to account for the depletion of metals onto grains. Finally, we set the turbulent velocity of the gas to 1.5 km/s (Cormier et al. 2019). The calculation is run until a visual extinction $A_V = 10$ mag is reached to ensure the full [C II] 158 μm luminosity is captured, since [C II] predominantly arises in PDRs (e.g. Abel et al. 2005). The SFR is measured – as a surface density Σ_SFR in $\mathrm{M}_\odot\ \mathrm{yr}^{-1}\ \mathrm{kpc}^{-2}$, since the geometry is plane parallel – through the incident UV continuum (i.e. the stellar radiation field at the illuminated face of the cloud, which is not attenuated by dust) at 1550 Å via the conversion given by Kennicutt & Evans (2012).[19]

In addition to these "vanilla" simulations of a H II region combined with a PDR, we also consider various deviations from the default scenario, whose impact will be discussed further in the next sections. Firstly, we varied the hydrogen density between $\log_{10}(n_\mathrm{H}\ [\mathrm{cm}^{-3}]) = 0.5$ and 3, in steps of 0.5. Secondly, we ran simulations that stop when molecules first start to form, changing the stopping criterion in CLOUDY to reaching a molecular hydrogen fraction of 10^{-6} instead of reaching a certain visual extinction, thereby effectively stripping away the PDR and leaving only the bare H II region. Thirdly, motivated by the observed α/Fe ratio at high redshift (e.g. Steidel et al. 2016), we considered models with an enhanced nebular α/Fe ratio, accomplished by scaling up the individual abundances of α elements (C, O, Ne, Mg, Si, and S) in the gas by a given factor $X_{\alpha/\mathrm{Fe,\,neb}}$. This results in an enhancement by the same factor of the α/Fe ratio relative to the default solar abundances:

$$X_{\alpha/\mathrm{Fe,\,neb}} = \frac{(\alpha/\mathrm{Fe})_\mathrm{neb}}{(\alpha/\mathrm{Fe})_\odot} = 10^{[\alpha/\mathrm{Fe}]_\mathrm{neb}},$$

such that X is simply the linear version of the logarithmic relative number density (bracket notation; Maiolino & Mannucci 2019). In this case, we additionally swap the solar metallicity case for $Z_* = 0.005\ \mathrm{Z}_\odot$. For our default α-enhancement of choice, $X_{\alpha/\mathrm{Fe,\,neb}} = 4$ (as seems appropriate from the findings discussed in the following Section 5.5), the effective nebular metallicities for α elements correspond to $Z_\mathrm{neb}/\mathrm{Z}_\odot = 0.02$, 0.2, and 0.8 (for $Z_*/\mathrm{Z}_\odot = 0.005$, 0.05, and 0.2, respectively). Fourthly, we similarly scaled down the carbon abundances by a certain factor, reflecting a sub-solar C/O ratio that may be appropriate in the early Universe, as will be discussed in Section 5.4. Finally, we increased the rate of cosmic rays (to 10× the CLOUDY default) that stimulates PDR heating and line intensities (notably that of [C II] 158 μm; e.g. Cormier

---

[16] The EW measurements of DGS sample will be presented in Kumari et al. (in prep.).

[17] We disregard the GOALS sample here, since their [O III] and Hβ EWs are not available.

[18] This circumvents the more extreme assumptions of a constant density throughout the H II region and PDR or constant pressure, which gives rise to a density discontinuity at the boundary layer between them.

[19] We note that the conversion of Kennicutt & Evans (2012) assumes a Kroupa & Weidner (2003) IMF, differing from BPASS that generates the incident radiation field with a Salpeter IMF. However, this is consistent with the conversion used for the observed SFRs (see Section 4); an additional translation between IMFs would therefore shift both models and observations by an equal amount.

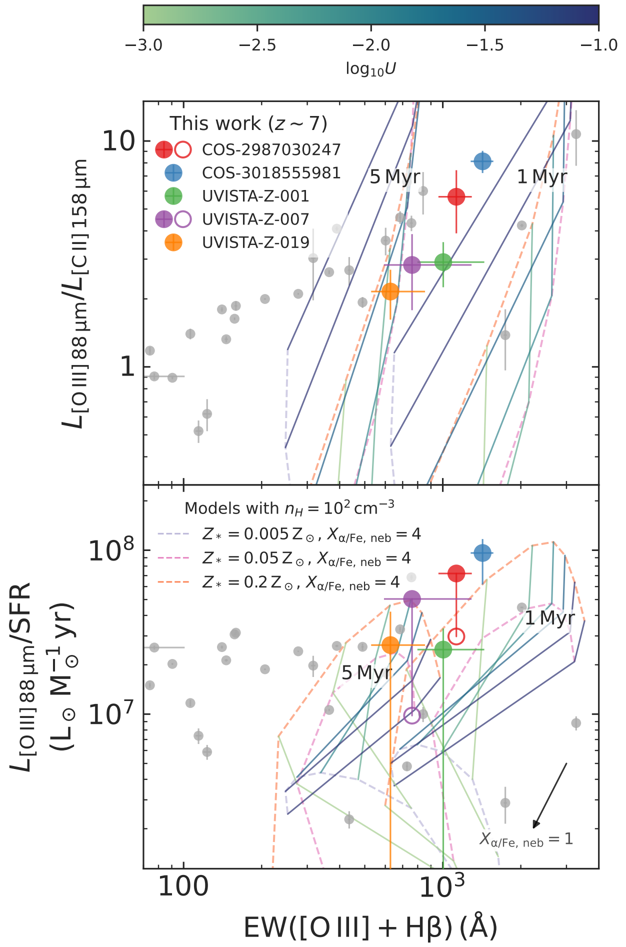

Figure 7. Relative strength of [O III] 88 μm with respect to [C II] 158 μm and SFR as a function of the EW of the optical [O III] and Hβ lines. Small grey circles are dwarf galaxies from the DGS (see Section 5.2), coloured circles are the five $z \sim 7$ galaxies considered in this work. Top panel: luminosity ratio of [O III] over [C II]. Grids of Cloudy models discussed in Section 5.3 with $n_\mathrm{H} = 10^2\,\mathrm{cm}^{-3}$ and stellar ages of 1 (right) and 5 Myr (left) are shown as grids, where the coloured dashed lines indicate a constant metallicity relative to Solar (see legend in the bottom panel). The gas in the main grids shown here has an α/Fe ratio enhanced by a factor 4 (see Section 5.3 for details). Solid lines of fixed ionisation parameter are coloured according to the colourbar on the top. Bottom panel: ratio of [O III] luminosity over SFR. The same Cloudy models as described above are overlaid. An arrow indicates the average shift of the models (~ 0.5 dex) if a solar α/Fe ratio is considered (i.e. $X_{\alpha/\mathrm{Fe,\,neb}} = 1$). The observations of [O III]/SFR at $z \sim 7$ (which, if they are limits, show unobscured SFR measurements with open circles) are mostly reproduced by Cloudy models, provided the metallicity is nearly at a solar level (Section 5.5).

et al. 2019). In the following, we discuss the theoretical interpretations that can be applied to observed [O III] 88 μm and [C II] 158 μm luminosities.

5.4 Insights on [O III] 88 μm and [C II] 158 μm

As discussed in Section 5.2, ALMA observations of the [O III] 88 μm and [C II] 158 μm lines in several EoR galaxies have hinted at high [O III]/[C II] ratios compared to local (U)LIRGs observed in GOALS and similar to local metal-poor dwarf galaxies from DGS with the highest EW([O III] + Hβ). From a theoretical perspective, there are many factors that could explain these high line ratios, if they are not purely caused by observational effects (as discussed in Section 5.2). Harikane et al. (2020) used Cloudy photoionisation models to show that the [O III]/[C II] luminosity ratio is expected to increase when increasing the ionisation parameter U, mostly through a decline of the [C II]/SFR ratio while [O III]/SFR remains fairly unchanged, consistent with the observational trends found for DGS galaxies in Section 5.2. In addition, the hydrogen density n_H is expected to play a role as the density approaches the critical density of [O III] ($510\,\mathrm{cm}^{-3}$), which is lower than that of [C II] produced in neutral gas ($\sim 2.8 \cdot 10^3\,\mathrm{cm}^{-3}$ when collision partners are atomic and molecular hydrogen; cf. Carilli & Walter 2013). However, in reality, the ISM is a complex, multi-phase environment; hence, [C II] and [O III] are typically expected to emerge largely from distinct gas reservoirs characterised by different densities (e.g. Katz et al. 2022; Pallottini et al. 2022).

The effect of varying carbon and oxygen abundances are also difficult to isolate. On its own, altering both abundances equally would affect the individual line strengths, but to first order leave their ratio unchanged. A secondary effect, however, is that a lower metallicity also decreases the dust-to-gas ratio (Galliano et al. 2018). Less dust allows UV photons to penetrate deeper into neutral gas, implying larger PDRs can form. Hence, with a lower metallicity, [C II] can become more luminous, which would lead to a suppressed [O III]/[C II] ratio. On the other hand, the global metallicity is also linked to the hardness of the stellar radiation field and the ionisation parameter, such that a low metallicity would be expected to lead to more highly ionised gas and thus a higher [O III]/[C II] ratio.

A recent study on a large number of simulated galaxies by Katz et al. (2022) instead argues for the need of a C/O abundance around 8× lower than solar in metal-poor systems, which would provide a direct explanation for the high [O III]/[C II] ratios. This can be interpreted as a result of rapid metal enrichment by low-metallicity core-collapse SNe responsible for producing the majority of oxygen, while type-Ia SNe and AGB stars, an important source of carbon enrichment, act on longer timescales (Arata et al. 2020; see also Maiolino & Mannucci 2019). A caveat of these results is that dust is neglected; still, Arata et al. (2020) report a similar anti-correlation between metallicity and [O III]/[C II] for simulated galaxies where dust is included, albeit in a smaller sample.

As discussed above, one-dimensional photoionisation codes are unlikely to capture the complexity of the ISM in its entirety, particularly in the early Universe. However, they are still useful as a first-order approximation of the strengths of emission lines given varying physical conditions. Indeed, any discrepancies between the predictions of such simulations and observed quantities can point towards their shortcomings. Therefore, as a reference, Cloudy models described in Section 5.3 are shown in the background of Figure 7. The models span the range of observed [O III]/[C II] ratios, albeit for high values of the ionisation parameter ($\log_{10} U > -1.5$). However, we note that if the simulated [O III] luminosity is indeed underestimated as suggested by the findings in Section 5.5, the same [O III]/[C II] ratio could be accomplished with a lower, more moderate ionisation parameter. In the case of the [O III]/[C II] ratio, varying the gas density does not produce significantly different results; as expected, stripping the PDR from the H II region, increasing the α enhancement, and lowering the C/O ratio all boost the [O III]/[C II] ratio, whereas enhancing cosmic ray background lowers [O III]/[C II].

The high luminosity ratios seen at high redshift, and in a subset of metal-poor dwarf galaxies, can be explained as coming from an elevated [O III] 88 μm luminosity, a [C II] 158 μm deficit, or a combination of both. Carniani et al. (2020) argued there is no significant [C II] deficit, as long as interferometric observations are properly set up to capture its full spatial extent. In line with these findings, we will show in the next section that photoionisation models appear to struggle to reproduce the (relative) strength of the observed [O III] 88 μm line, pointing towards an [O III] enhancement causing the elevated [O III]/[C II] ratios (even though [C II] seems to be responsible for the correlation with EW of the optical lines more than [O III], as discussed in Section 5.2).

5.5 Optical and FIR lines of [O III]

In the bottom panel of Figure 7, results from the Cloudy models discussed above (Section 5.3) are shown in the plane of relative strengths of key [O III] emission lines, [O III] 88 μm and the [O III] $\lambda\lambda\,4960, 5008$ Å lines. Because we infer the rest-frame optical [O III] strength from the *Spitzer*/IRAC [3.6] − [4.5] colour, we estimate the line strength as the combined EW of [O III] $\lambda\lambda\,4960, 5008$ Å and Hβ lines, denoted as EW([O III] + Hβ) here, while we estimate the FIR [O III] 88 μm line strength as $L_{\text{[O III] 88 μm}}/\text{SFR}$. Using these relative luminosities allows us to compare local and high-redshift galaxies on a more equal footing. Additionally, we note dust attenuation (and hence our choice of a $A_V = 10$ mag stopping criterion) is not of major importance here, since the [O III] $\lambda\,5008$ Å line and stellar continuum flux are, to first order, expected to be affected equally, which cancels out in the EW, while the [O III] 88 μm line is optically thin.

Observations of all metal-poor dwarf galaxies from the DGS are included in addition to the five $z \sim 7$ star-forming galaxies considered in this work, for which we set lower limits using the unobscured SFR only if no dust continuum was detected. All measurements shown in the bottom panel of Figure 7, except for a few dwarf galaxies with low EWs, favour models with a young stellar population for the relative strengths of both [O III] lines to be successfully reproduced. Observations of the $z \sim 7$ galaxies in particular appear to require a young stellar population of between 1 and 5 Myr. Lower gas densities (e.g. $n_\text{H} \sim 10^{0.5}\,\text{cm}^{-3}$) slightly increase the relative [O III] luminosity and the EW of the optical lines (both by around 0.2 dex), though the models with $n_\text{H} \sim 10^{2}\,\text{cm}^{-3}$ shown here coincide better with the data locus of the DGS and high-redshift galaxies combined. Higher gas densities (e.g. $n_\text{H} \sim 10^{2.5}\,\text{cm}^{-3}$), as sometimes observed in local high-redshift analogues (e.g. Berg et al. 2016) decrease the relative [O III] luminosity by ∼ 0.3 dex. The presence of PDRs and cosmic rays have a largely negligible impact.

Perhaps most remarkable is the fact that – even with lower gas densities – the observations seem to require a relatively high metallicity (in line with the findings of Harikane et al. 2020). We note that simulations with a very young stellar population of 1 Myr and fully solar metallicity (i.e. $Z_* = Z_\text{neb} = \text{Z}_\odot$; not shown here) are just able to recover the relative [O III] 88 μm luminosity for very high ionisation parameters but fail to simultaneously replicate the EWs of the optical lines for the two COSMOS sources in particular. Out of a large range of models, we find the most consistent are those where specifically α elements have near-solar nebular abundances, i.e. $[\alpha/\text{H}]_\text{neb} \sim 0$, as illustrated in the bottom panel of Figure 7 by the arrow, indicating the ∼ 0.5 dex downwards shift of the grid when $X_{\alpha/\text{Fe, neb}} = 1$ as opposed to $X_{\alpha/\text{Fe, neb}} = 4$ as shown. This scenario may be expected from a rapid metal enrichment of the ISM that causes the stellar metallicity to lag behind the nebular metallicity. We note such high metal abundances corroborate the finding of a seemingly high dust-to-stellar mass ratio discussed in Section 4.2 and modest gas-to-dust mass ratio discussed in Section 5.1.

Interestingly, a metallicity calibration employing the [O III] 88 μm line suggested by Jones et al. (2020b) indeed predicts relatively high metallicities given the [O III] 88 μm luminosities of the $z \sim 7$ galaxies; remarkably, this yields a super-solar value of $12 + \log\,(\text{O/H}) \simeq 8.72$ for COS-3018555981 (solar abundance being $12 + \log\,(\text{O/H})_\odot = 8.69$; Asplund et al. 2009), as has been reported (albeit for higher-mass systems) in a number of recent works (Litke et al. 2022, and references therein). Yet such (α-element) abundances are exceptionally high compared to what may be expected for young star-forming galaxies less than a billion years after the Big Bang. Even when assuming there is no evolution in the mass-metallicity relation (MZR) beyond a redshift of $z \sim 3$ (while evidence of an underlying evolution up to $z \sim 5$ is already emerging; Witstok et al. 2021), a solar metallicity poses a significant offset (around 0.5 dex or a factor of ∼ 3) from the predicted metallicity of a galaxy with $M_* \sim 10^9\,\text{M}_\odot$ (Sanders et al. 2021).

Relatively high [O III] 88 μm luminosities have previously been observed in local metal-poor galaxies, as noted by for example Lebouteiller et al. (2012) in the case of the Large Magellanic Cloud (LMC) and Cormier et al. (2015, 2019) for the DGS galaxies. The models of Lebouteiller et al. (2012) point towards the need of a relatively cool ($T < 10\,000$ K) ionised gas, consistent with our metal-rich models that have more efficient cooling: for solar metallicity, for instance, $T \sim 8000$ K in the H II region, as opposed to $T \gtrsim 10\,000$ K for $Z < Z_\odot$. On the contrary, the metal-poor dwarf galaxies from the DGS have directly observed nebular metallicities of $Z_\text{neb} \lesssim 0.3\,\text{Z}_\odot$, which are instead coupled with high temperatures, $15\,000\,\text{K} \lesssim T \lesssim 20\,000$ K (e.g. Izotov et al. 1990, 1997; Izotov & Thuan 1998; Guseva et al. 2000), as would be expected given the principal role of heavy elements as a cooling agent. This indicates that photoionisation models seem to be missing a key ingredient to replicate the strength of the [O III] 88 μm line.

One of the main assumptions of our simple, one-dimensional photoionisation model is to consider an ionisation-bounded nebula (with a smooth density profile and constant metallicity), while – as noted in Section 5.4 – this is likely not entirely correct, given for instance the role star-forming galaxies are thought to play in reionising the neutral IGM (Robertson 2021). Indeed, Cormier et al. (2015, 2019) argue for the presence of escape channels which allow ionising radiation to escape H II regions, leading to a large volume filling factor of diffuse (i.e. with density comparable to or lower than the critical density of [O III] 88 μm, $510\,\text{cm}^{-3}$) ionised gas. Another possibility for the discrepancy would be that, in estimating the relative [O III] luminosity, the observed SFR is underestimated, for example by considering dust temperatures lower than what they are in reality (in particular COS-3018555981; cf. Section 4.3); however, this seems unlikely in the case of COS-2987030247 and UVISTA-Z-007 for which we do not detect dust continuum emission (and thus have an upper limit on the obscured SFR).

5.6 Spatially resolved emission line analysis

In the previous sections, we have discussed the interpretation of line strengths and their ratios globally (i.e. integrated across the galaxy). However, the ISM is known to be complex and inhomogeneous, especially at high redshift (Vallini et al. 2021; Pallottini et al. 2022). Here, we will instead briefly discuss detections of the [C II] 158 μm and [O III] 88 μm lines on a spatially resolved scale.

Previous works have already demonstrated significant offsets (as well as different sizes) between the rest-frame UV and [C II] 158

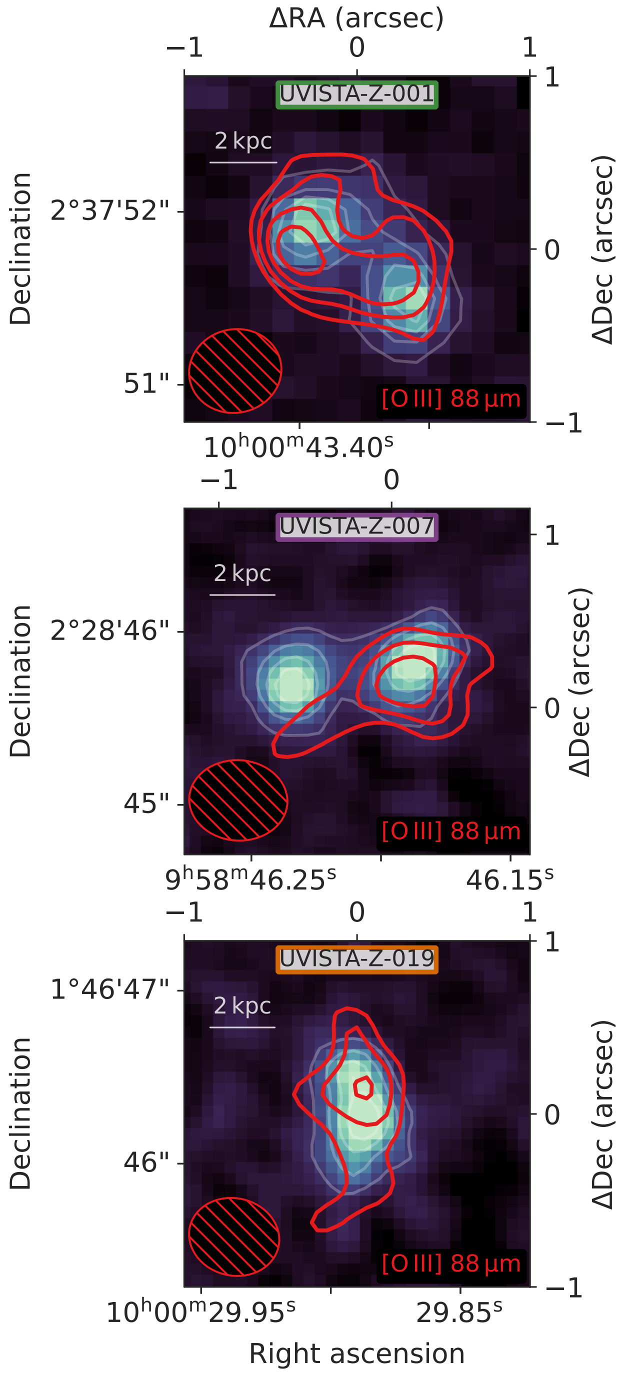

Figure 8. *HST* images of the rest-frame UV (in the JH_{140} band; Section 2.3) overlaid by contours of the [O III] 88 μm line (achieving a ~ 0.4″ resolution with natural weighting; see Table 2) of UVISTA-Z-001 (top panel), UVISTA-Z-007 (middle panel) and UVISTA-Z-019 (bottom panel). Red [O III] contours are drawn from 3σ and going up in steps of 1σ. The top left indicates a physical scale of 2 kpc. Beam sizes for [O III] are indicated in the bottom left.

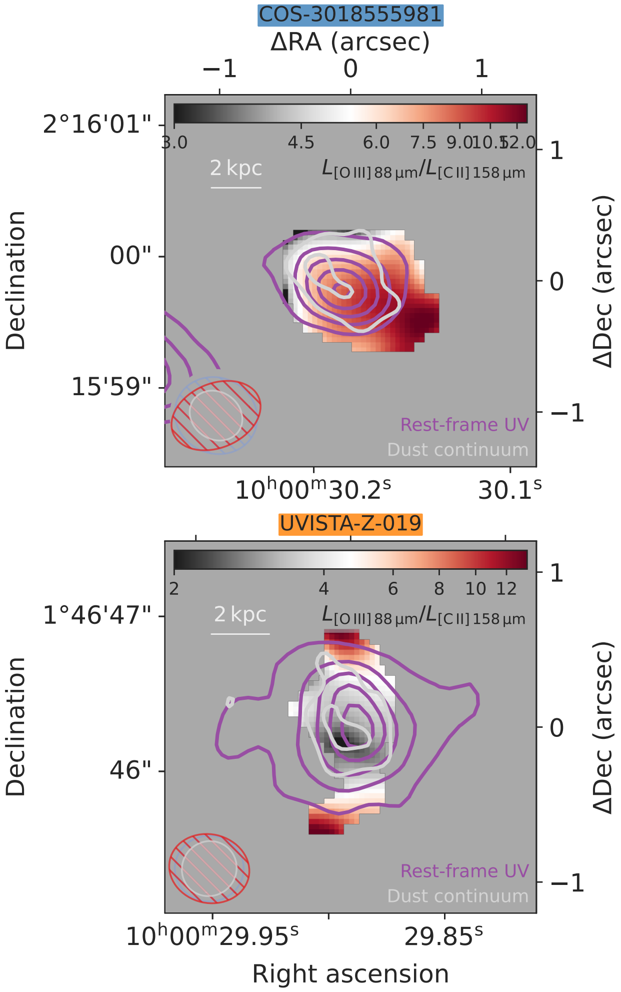

Figure 9. Line ratio maps of the [O III] 88 μm and [C II] 158 μm lines for COS-3018555981 (top panel) and UVISTA-Z-019 (bottom panel), where imaging parameters have been chosen to match beam sizes (see Table 2). Light grey contours are drawn for the dust continuum (at ~ 160 μm, with natural weighting scheme; Section 5.6 for details), starting from 3σ and going up in steps of 2σ. Purple contours are drawn for the *HST* imaging (Section 2.3) of the rest-frame UV (convolved to match the dust continuum PSF), starting from 5σ and going up in steps of 5σ. Beam sizes are indicated in the bottom left (partially hiding a foreground source in the *HST* imaging of COS-3018555981); the top left indicates a physical scale of 2 kpc. There is tentative evidence for spatial variation in the [O III]/[C II] ratio, including a gradient with the lowest [O III]/[C II] values seeming to align with the location of the dust emission in COS-3018555981.

μm emission (e.g. Maiolino et al. 2015; Carniani et al. 2018a,b). Here, we show a detailed comparison between the UV and [O III] 88 μm emission in Figure 8 for all three UVISTA sources, where ALMA achieves a moderately high spatial resolution (with a beam size of ~0.4″). Despite good agreement between the compact morphology of both the rest-frame UV and the [O III] contours, there are signs of minor misalignment: most notably, the observed [O III] signal is clearly centred on the western component of UVISTA-Z-007, whereas the eastern component distinctly lacks [O III] emission of comparable strength. We quantified this by fitting separate two-dimensional Gaussian components to the *HST* images, resulting in two components with very similar integrated UV luminosities

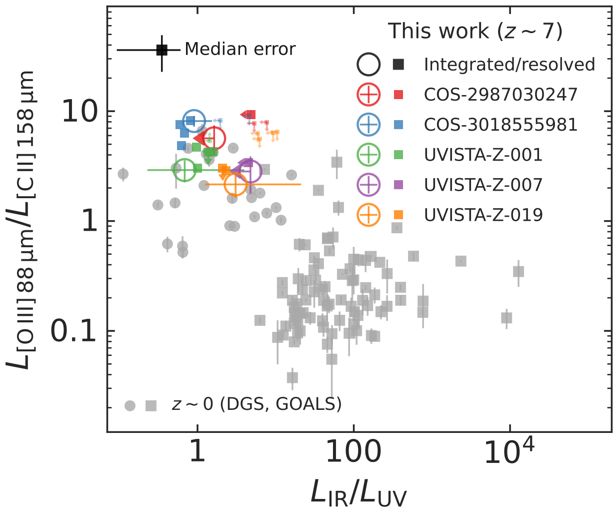

Figure 10. Sequence of the [O III] 88 µm to [C II] 158 µm ratio as a function of $L_\mathrm{IR}/L_\mathrm{UV}$. Global measurements of the DGS and GOALS samples are shown, as are the five $z \sim 7$ star-forming galaxies discussed in this work. Furthermore, spatially resolved ratios extracted from individual regions across all five sources (see Appendix B for details) are shown as squares (smaller squares if we can only set 2σ limits on both ratios). For clarity, error bars of the spatially resolved measurements are not shown; the median error of these points is indicated by the black square in the top left.

of around $7 \cdot 10^{10}\,\mathrm{L}_\odot$ (their ratio being ~ 1.1) at a separation of $\sim 0.71''$ or 3.8 kpc, whereas the luminosity ratio of the [O III] 88 µm line compared to the UV, $L_{[\mathrm{O\,III}]}/L_\mathrm{UV}$, differs by almost a factor two (measured as $(1.2 \pm 0.6) \cdot 10^{-3}$ and $(2.2 \pm 0.6) \cdot 10^{-3}$ for the eastern and western components, respectively) in a region encompassing twice the FWHMs. As indicated by its kinematics, this is likely an ongoing galaxy merger (Schouws et al. 2022a). A similar double-component UV morphology is seen in UVISTA-Z-001, although the two components separated by $\sim 0.68''$ or 3.5 kpc display a more equal $L_{[\mathrm{O\,III}]}/L_\mathrm{UV}$ ratio (respectively $(6.3 \pm 0.2) \cdot 10^{-3}$ and $(5.0 \pm 0.2) \cdot 10^{-3}$ for the eastern and western components).

To investigate such apparent peculiarities in the [O III] morphology further, we have regridded images of the [O III] 88 µm to [C II] 158 µm lines (integrated over the FWHM centred on the line, created from imaging parameters that have been chosen to match beam sizes; see Table 2) to a common coordinate mesh to create maps of their ratio in regions where both lines are detected with at least 3σ so that $\mathrm{SNR}_{[\mathrm{O\,III}]/[\mathrm{C\,II}]} \gtrsim 2$. On the scales down to which we resolve the lines (around 2 to 3 kpc), the line ratio can indeed also vary significantly across the galaxy, as illustrated by the example of COS-3018555981 in the top panel of Figure 9, where the line ratio varies locally from the order of unity up to more than 10. The ratio map of UVISTA-Z-019, shown in the bottom panel of Figure 9, also reveals indications of a spatially varying ratio (on the order of 2 to 4 in the centre). It further shows an enhanced ratio in the northern and southern outskirts; although the SNR will be reduced in these regions, this does not appear to be due to noise (demonstrated by spectra extracted from manually placed beams as in Appendix B). It lacks strong evidence for a clear gradient, however, as is the case for the other three sources not shown here (due in part to a lack of resolution and/or overlap in the [O III] and [C II] lines).

The dust continuum and rest-frame UV imaging, shown by overlaid contours, are matched in PSF by convolving the *HST* imaging with a kernel found by the Richardson-Lucy algorithm. To maximise SNR, we show the continuum images created under a natural weighting scheme (see Section 2.2.2), which are therefore at slightly higher resolution than [O III] and [C II]. Interestingly, the location of the dust continuum seem to mostly coincide with the side of the galaxy which shows a lower [O III]/[C II] ratio. Given SNR of the continuum detection in this case ($\sim 10\sigma$; see Figure 1 and Table 3) and the beam size ($\sim 0.7''$), we estimate the positional accuracy to be $\sim 0.1''$, indicating the observed offset and alignment with the northwestern region is significant.[20] Given the link between a high [O III]/[C II] ratio on the one hand and a starburst's young age or high ionisation parameter on the other (as shown in Section 5.4; see also e.g. Vallini et al. 2021), this suggests the relatively unobscured region in the southeast with high [O III]/[C II] may be experiencing a more recent and/or intense burst of star formation. In contrast, it appears to be inconsistent with a scenario of UV-bright regions being slightly more evolved sites of star formation, where SNe (or other types of feedback) have been able to clear out the dust. A lack of dust implies the gas is likely low in metallicity, potentially linked with an inflow of pristine gas triggering the burst of star formation.

This tentative interplay between the FIR line ratio and degree of dust obscuration is further tested in Figure 10, where we show measurements of [O III]/[C II] as a function of the infrared excess (IRX), $\mathrm{IRX} \equiv L_\mathrm{IR}/L_\mathrm{UV}$. Global measurements of the DGS and GOALS samples are shown, as are the five $z \sim 7$ star-forming galaxies discussed in this work. In addition, we placed individual beams across all five sources to measure these quantities on a spatially resolved scale (see Appendix B for details).

We considered measurements only when exceeding the estimated sensitivity by at least 2σ, setting upper or lower limits (2σ) if only one of the lines and/or continua shows a detectable signal. These measurements are clearly pushing the SNR of the data since a lot of points are in fact limits, mostly due to a lack of significant dust continuum (see also the large median error bar on non-limits). As may be expected from the data with the highest SNR, spatially resolved measurements of COS-3018555981 do yield four significant measurements spanning a [O III]/[C II] ratio from 5 to 8 and IRX from 0.5 to 0.9 (both with a spread of around 0.2 dex). Three measurements of UVISTA-Z-001 are similarly spread out (~ 0.2 dex) at slightly lower [O III]/[C II] ratio (3 to 5) and higher IRX (1 to 1.4). For UVISTA-Z-019, two beams have confidently detected IRX values, with one [O III]/[C II] detection and one upper limit (both approximately ~ 2 and ~ 3, respectively). For several beams placed over COS-2987030247, $\mathrm{IRX} \lesssim 5$, while the [O III]/[C II] ratio in one beam is measured to be ~ 9.

Combined with the data obtained on a global scale, there is a tentative negative correlation where a galaxy (region) with high IRX tends to have a lower [O III]/[C II] ratio. This fits in with the picture sketched above, in which young and/or intense bursts of star formation, accompanied with a large [O III]/[C II] ratio, occur in unobscured and hence likely metal-poor regions, whereas obscured star formation is linked to more moderate line ratios.

6 SUMMARY AND CONCLUSIONS

We have presented ALMA observations of the [O III] 88 µm line in five $z \sim 7$ star-forming (Lyman-break) galaxies that have previously

---

[20] For this estimate, we consulted Section 10.5.2 of the ALMA Technical Handbook (Cortes et al. 2020).

been spectroscopically confirmed by ALMA via their [C ii] 158 µm line, each yielding a confident [O iii] detection (SNR > 5). We complement these observations with new *HST* rest-frame UV imaging of two of the sources. Furthermore, we have presented a non-detection of [N ii] 205 µm in COS-2987030247 in addition to the corresponding dust continuum measurements around each emission line. We summarise our findings as follows:

- For two sources, COS-2987030247 and UVISTA-Z-007, we do not confidently detect dust continuum emission in any ALMA band. For COS-3018555981 and UVISTA-Z-019, however, we have significant detections at ∼ 160 µm yet we do not detect the continuum at ∼ 90 µm. In UVISTA-Z-001, we detect compact ∼ 90 µm continuum emission in band 8, in contrast to a more extended dust reservoir observed at ∼ 160 µm. The compact component has a seemingly typical dust temperature of ∼ 60 K, while the extended component is likely colder. The dust-continuum measurements of COS-3018555981 also favour a low dust temperature coupled with a high dust mass: the dust temperature, nominally $T_{\rm dust} = 29^{+9}_{-5}$ K (or $T_{\rm dust} < 48$ K at 95% confidence) compared to a CMB temperature of 21 K at $z \sim 7$, may be lower than those of all other EoR sources known, while its dust mass implies a high stellar metallicity yield (accompanied by a top-heavy IMF) and may point towards the need of other dust production and/or growth mechanisms beyond SNe.
- The non-detection of [N ii] 205 µm in COS-2987030247 allows us to set a lower limit on the [C ii]/[N ii] ratio ($L_{[\rm C\,II]}/L_{[\rm N\,II]} > 4.8$ at 3σ), which is fully consistent with [C ii] production in a PDR-like medium, and renders H ii regions the unlikely primary origin of the [C ii] emission (except in a more extreme physical environment with low metallicity, high ionisation parameter, and/or high gas density).
- We find modest ratios of [O iii] 88 µm to [C ii] 158 µm (around 2 to 3) for the sources with moderate EWs of the optical [O iii] and Hβ lines (rest-frame EW ∼ 700 Å) while the ratio is comparatively higher (6 to 8) for the sources with more extreme EWs (EW > 1000 Å), consistent with a positive correlation between EW and [O iii]/[C ii] seen in local metal-poor dwarf galaxies.
- Through the photoionisation code Cloudy, we find that a young stellar population embedded in a nebula of typical density with a high ionisation parameter appears an appropriate model of the physical environment in which the FIR emission lines originate. Surprisingly, however, the modelled nebular emission barely reproduces the observed strength of the [O iii] 88 µm line in sources with high EW([O iii] + Hβ). Moreover, we find the Cloudy modelling only recovers the observed [O iii] 88 µm line strength when the α/Fe ratio relative to solar is raised by increasing the abundances of α elements, leading to a relatively cool ionised gas ($T \sim 8000$ K), in contrast to direct measurements of potential local analogues (i.e. metal-poor dwarf galaxies). This suggests luminous LBGs at $z \sim 7$ might be more chemically enriched than is often assumed, or else, that significant [O iii] 88 µm emission emerges from a low density, moderately cool medium outside of the modelled H ii regions.
- We find the [O iii]/[C ii] ratio shows a tentative anti-correlation with the degree of dust obscuration (measured through the IRX) on spatially resolved scales, similar to the trend seen in the local Universe on global scales of metal-poor dwarf galaxies and (U)LIRG starburst galaxies. This suggests a large [O iii]/[C ii] ratio accompanies young and/or intense bursts of star formation, which occur in unobscured and hence likely metal-poor regions.

DATA AVAILABILITY

HST data underlying this article are available in the MAST archive at 10.17909/6gya-3b10 (GO 13793), 10.17909/T9-JHSF-M392 (GO 16506) and from `https://archive.stsci.edu/prepds/3d-hst/` (the 3D-HST Treasury Program). *Gaia* data may be obtained from `https://gea.esac.esa.int/archive/`. The ALMA data underlying this article are available in the ALMA science archive at `https://almascience.eso.org/asax/` under by the following project codes (see also Table 2):

- ADS/JAO.ALMA#2015.1.01111.S
- ADS/JAO.ALMA#2018.1.01359.S
- ADS/JAO.ALMA#2018.1.00429.S
- ADS/JAO.ALMA#2018.1.01551.S
- ADS/JAO.ALMA#2017.1.00604.S
- ADS/JAO.ALMA#2015.1.00540.S
- ADS/JAO.ALMA#2018.1.00085.S
- ADS/JAO.ALMA#2018.1.00933.S
- ADS/JAO.ALMA#2019.1.01611.S
- ADS/JAO.ALMA#2019.1.01524.S
- ADS/JAO.ALMA#2018.1.00085.S
- ADS/JAO.ALMA#2019.1.01611.S

Reduced data underlying this article will be shared on reasonable request to the corresponding author.

ACKNOWLEDGEMENTS

We are grateful to Caitlin Casey and Seiji Fujimoto for insightful discussions on the reduction and interpretation of the ALMA measurements. We furthermore thank the anonymous referee for their comments. JW, RS, RM, and GCJ acknowledge support from the ERC Advanced Grant 695671, "QUENCH", and the Fondation MERAC. RS acknowledges support from a Netherlands Organisation for Scientific Research (NWO) Rubicon grant, project number 680-50-1518, and an STFC Ernest Rutherford Fellowship (ST/S004831/1). RM also acknowledges funding from a research professorship from the Royal Society. MA acknowledges support from FONDECYT grant 1211951, CONICYT+PCI+INSTITUTO MAX PLANCK DE ASTRONOMIA MPG190030, CONICYT+PCI+REDES 190194 and ANID BASAL project FB210003. JAH gratefully acknowledges support of the VIDI research program with project number 639-042-611, which is (partly) financed by the NWO. This work has extensively used casa (McMullin et al. 2007), developed by an international consortium of scientists based at the National Radio Astronomical Observatory (NRAO), the European Southern Observatory (ESO), the National Astronomical Observatory of Japan (NAOJ), the Academia Sinica Institute of Astronomy and Astrophysics (ASIAA), CSIRO Astronomy and Space Science (CSIRO/CASS), and the Netherlands Institute for Radio Astronomy (ASTRON), under the guidance of NRAO. Furthermore, it has used the following packages in python: the SciPy library (Jones et al. 2001), its packages NumPy (Van der Walt et al. 2011) and Matplotlib (Hunter 2007), the Astropy (Astropy Collaboration et al. 2013, 2018), pymultinest (Feroz et al. 2009; Buchner et al. 2014), and DrizzlePac packages (`https://www.stsci.edu/scientific-community/software/drizzlepac.html`.

This work was based on observations taken by the Atacama Large Millimeter/submillimeter Array (ALMA). ALMA is a partnership of ESO (representing its member states), NSF (USA) and NINS (Japan), together with NRC (Canada), MOST and ASIAA

(Taiwan), and KASI (Republic of Korea), in cooperation with the Republic of Chile. The Joint ALMA Observatory is operated by ESO, AUI/NRAO and NAOJ.

This work was furthermore partially based on new observations made with the NASA/ESA *Hubble Space Telescope* (*HST*), obtained at the Space Telescope Science Institute (STScI), which is operated by the Association of Universities for Research in Astronomy, Inc., under NASA contract NAS 5-26555. These observations are associated with programme #16506. Additionally, *HST* archival data was obtained from the data archive at the STScI. STScI is operated by the Association of Universities for Research in Astronomy, Inc. under NASA contract NAS 5-26555.

Finally, this work has made use of data from the European Space Agency (ESA) mission *Gaia* (`https://www.cosmos.esa.int/gaia`), processed by the *Gaia* Data Processing and Analysis Consortium (DPAC, `https://www.cosmos.esa.int/web/gaia/dpac/consortium`). Funding for the DPAC has been provided by national institutions, in particular the institutions participating in the *Gaia* Multilateral Agreement.

REFERENCES

Abel N. P., Ferland G. J., Shaw G., Troland T. H., O'Dell C. R., 2005, in American Astronomical Society Meeting Abstracts. p. 81.17
Akins H., et al., 2022, preprint, (`arXiv:2206.06939`)
Arata S., Yajima H., Nagamine K., Abe M., Khochfar S., 2020, MNRAS, 498, 5541
Asplund M., Grevesse N., Sauval A. J., Scott P., 2009, ARA&A, 47, 481
Astropy Collaboration et al., 2013, A&A, 558, A33
Astropy Collaboration et al., 2018, AJ, 156, 123
Bakx T. J. L. C., et al., 2020, MNRAS, 493, 4294
Bakx T. J. L. C., et al., 2021, MNRAS, 508, L58
Behrens C., Pallottini A., Ferrara A., Gallerani S., Vallini L., 2018, MNRAS, 477, 552
Berg D. A., Skillman E. D., Henry R. B. C., Erb D. K., Carigi L., 2016, ApJ, 827, 126
Bouwens R., et al., 2020, ApJ, 902, 112
Bouwens R. J., et al., 2021, AJ, 162, 47
Bouwens R. J., et al., 2022, ApJ, 931, 160
Bowler R. A. A., Dunlop J. S., McLure R. J., McLeod D. J., 2017, MNRAS, 466, 3612
Bowler R. A. A., Bourne N., Dunlop J. S., McLure R. J., McLeod D. J., 2018, MNRAS, 481, 1631
Bowler R. A. A., Cullen F., McLure R. J., Dunlop J. S., Avison A., 2022, MNRAS, 510, 5088
Braatz J., Biggs A., Sanhueza P., Corvillon A., 2021, ALMA Cycle 8 2021 Proposer's Guide. `https://almascience.eso.org/documents-and-tools/cycle8/alma-proposers-guide`
Buchner J., et al., 2014, A&A, 564, A125
Carilli C. L., Walter F., 2013, ARA&A, 51, 105
Carniani S., et al., 2018a, MNRAS, 478, 1170
Carniani S., Maiolino R., Smit R., Amorín R., 2018b, ApJ, 854, L7
Carniani S., et al., 2020, MNRAS, 499, 5136
Casey C. M., 2012, MNRAS, 425, 3094
Casey C. M., Narayanan D., Cooray A., 2014, Phys. Rep., 541, 45
Casey C. M., et al., 2021, ApJ, 923, 215
Chabrier G., 2003, PASP, 115, 763
Chen L.-H., Hirashita H., Hou K.-C., Aoyama S., Shimizu I., Nagamine K., 2018, MNRAS, 474, 1545
Clements D. L., Dunne L., Eales S., 2010, MNRAS, 403, 274
Cormier D., et al., 2015, A&A, 578, A53
Cormier D., et al., 2019, A&A, 626, A23
Cortes P. C., et al., 2020, ALMA Technical Handbook. `https://almascience.eso.org/documents-and-tools/cycle8/alma-technical-handbook`
Cortzen I., et al., 2020, A&A, 634, L14
da Cunha E., et al., 2013, ApJ, 766, 13
Cunningham D. J. M., et al., 2020, MNRAS, 494, 4090
Dayal P., Ferrara A., 2018, Phys. Rep., 780, 1
De Looze I., et al., 2014, A&A, 568, A62
Decarli R., et al., 2014, ApJ, 782, L17
Díaz-Santos T., et al., 2017, ApJ, 846, 32
Draine B. T., 2006, ApJ, 636, 1114
Drew P. M., Casey C. M., 2022, ApJ, 930, 142
Eldridge J. J., Stanway E. R., Xiao L., McClelland L. A. S., Taylor G., Ng M., Greis S. M. L., Bray J. C., 2017, Publ. Astron. Soc. Australia, 34, e058
Endsley R., Stark D. P., Chevallard J., Charlot S., 2021, MNRAS, 500, 5229
Faisst A. L., Fudamoto Y., Oesch P. A., Scoville N., Riechers D. A., Pavesi R., Capak P., 2020, MNRAS, 498, 4192
Ferland G. J., et al., 2017, Rev. Mex. Astron. Astrofis., 53, 385
Feroz F., Hobson M. P., Bridges M., 2009, MNRAS, 398, 1601
Ferrara A., Vallini L., Pallottini A., Gallerani S., Carniani S., Kohandel M., Decataldo D., Behrens C., 2019, MNRAS, 489, 1
Franco M., et al., 2018, A&A, 620, A152
Fruchter A. S., Hook R. N., 2002, PASP, 114, 144
Fudamoto Y., et al., 2021, Nature, 597, 489
Gaia Collaboration et al., 2016, A&A, 595, A1
Gaia Collaboration et al., 2021, A&A, 649, A1
Galliano F., Galametz M., Jones A. P., 2018, ARA&A, 56, 673
Grogin N. A., et al., 2011, ApJS, 197, 35
Groves B. A., Dopita M. A., Sutherland R. S., 2004, ApJS, 153, 75
Guseva N. G., Izotov Y. I., Thuan T. X., 2000, ApJ, 531, 776
Harikane Y., et al., 2020, ApJ, 896, 93
Hashimoto T., et al., 2019, PASJ, 71, 71
Heintz K. E., Watson D., Oesch P. A., Narayanan D., Madden S. C., 2021, ApJ, 922, 147
Heintz K. E., et al., 2022, preprint, (`arXiv:2206.07763`)
Hirashita H., Ferrara A., Dayal P., Ouchi M., 2014, MNRAS, 443, 1704
Hodge J. A., da Cunha E., 2020, Royal Society Open Science, 7, 200556
Hollenbach D. J., Tielens A. G. G. M., 1999, Reviews of Modern Physics, 71, 173
Hunter J. D., 2007, Computing in Science & Engineering, 9, 90
Inoue A. K., et al., 2016, Science, 352, 1559
Inoue A. K., Hashimoto T., Chihara H., Koike C., 2020, MNRAS, 495, 1577
Izotov Y. I., Thuan T. X., 1998, ApJ, 500, 188
Izotov I. I., Guseva N. G., Lipovetskii V. A., Kniazev A. I., Stepanian J. A., 1990, Nature, 343, 238
Izotov Y. I., Thuan T. X., Lipovetsky V. A., 1997, ApJS, 108, 1
Jones E., Oliphant T., Peterson P., et al., 2001, SciPy: Open source scientific tools for Python, `http://www.scipy.org/`
Jones G. C., Maiolino R., Caselli P., Carniani S., 2020a, MNRAS, 498, 4109
Jones T., Sanders R., Roberts-Borsani G., Ellis R. S., Laporte N., Treu T., Harikane Y., 2020b, ApJ, 903, 150
Jones G. C., et al., 2021, MNRAS, 507, 3540
Katz H., et al., 2019, MNRAS, 487, 5902
Katz H., et al., 2020, MNRAS, 498, 164
Katz H., et al., 2022, MNRAS, 510, 5603
Kennicutt R. C., Evans N. J., 2012, ARA&A, 50, 531
Kewley L. J., Nicholls D. C., Sutherland R. S., 2019, ARA&A, 57, 511
Knudsen K. K., Watson D., Frayer D., Christensen L., Gallazzi A., Michałowski M. J., Richard J., Zavala J., 2017, MNRAS, 466, 138
Koekemoer A. M., et al., 2011, ApJS, 197, 36
Kroupa P., 2001, MNRAS, 322, 231
Kroupa P., Weidner C., 2003, ApJ, 598, 1076
Laporte N., et al., 2017, ApJ, 837, L21
Lebouteiller V., et al., 2012, A&A, 548, A91
Leonova E., et al., 2021, preprint, (`arXiv:2112.07675`)
Leśniewska A., Michałowski M. J., 2019, A&A, 624, L13
Liang L., et al., 2019, MNRAS, 489, 1397
Litke K. C., et al., 2022, ApJ, 928, 179
Ma X., et al., 2019, MNRAS, 487, 1844
Madau P., Dickinson M., 2014, ARA&A, 52, 415

Madden S. C., et al., 2013, PASP, 125, 600
Madden S. C., et al., 2014, PASP, 126, 1079
Maiolino R., Mannucci F., 2019, A&ARv, 27, 3
Maiolino R., et al., 2015, MNRAS, 452, 54
Mancini M., Schneider R., Graziani L., Valiante R., Dayal P., Maio U., Ciardi B., Hunt L. K., 2015, MNRAS, 451, L70
Manning S. M., et al., 2022, ApJ, 925, 23
Mateo M. L., 1998, ARA&A, 36, 435
McCracken H. J., et al., 2012, A&A, 544, A156
McMullin J. P., Waters B., Schiebel D., Young W., Golap K., 2007, in Shaw R. A., Hill F., Bell D. J., eds, Astronomical Society of the Pacific Conference Series Vol. 376, Astronomical Data Analysis Software and Systems XVI. p. 127
Michałowski M. J., 2015, A&A, 577, A80
Nagao T., Maiolino R., De Breuck C., Caselli P., Hatsukade B., Saigo K., 2012, A&A, 542, L34
Nozawa T., Kozasa T., Umeda H., Maeda K., Nomoto K., 2003, ApJ, 598, 785
Oke J. B., Gunn J. E., 1983, ApJ, 266, 713
Pallottini A., et al., 2019, MNRAS, 487, 1689
Pallottini A., et al., 2022, MNRAS, 513, 5621
Pavesi R., et al., 2016, ApJ, 832, 151
Pavesi R., Riechers D. A., Faisst A. L., Stacey G. J., Capak P. L., 2019, ApJ, 882, 168
Planck M., 1901, Annalen der Physik, 309, 553
Rémy-Ruyer A., et al., 2014, A&A, 563, A31
Reuter C., et al., 2020, ApJ, 902, 78
Robertson B. E., 2021, preprint, (`arXiv:2110.13160`)
Salpeter E. E., 1955, ApJ, 121, 161
Sanders D. B., Mirabel I. F., 1996, ARA&A, 34, 749
Sanders R. L., et al., 2016, ApJ, 816, 23
Sanders R. L., et al., 2021, ApJ, 914, 19
Sawicki M., 2012, PASP, 124, 1208
Schneider R., Omukai K., Inoue A. K., Ferrara A., 2006, MNRAS, 369, 1437
Schouws S., et al., 2022a, preprint, (`arXiv:2202.04080`)
Schouws S., et al., 2022b, ApJ, 928, 31
Schreiber C., Elbaz D., Pannella M., Ciesla L., Wang T., Franco M., 2018, A&A, 609, A30
Scoville N., et al., 2017, ApJ, 837, 150
Skelton R. E., et al., 2014, ApJS, 214, 24
Smit R., et al., 2015, ApJ, 801, 122
Smit R., et al., 2018, Nature, 553, 178
Sommovigo L., Ferrara A., Pallottini A., Carniani S., Gallerani S., Decataldo D., 2020, MNRAS, 497, 956
Sommovigo L., et al., 2022, MNRAS, 513, 3122
Stanway E. R., Eldridge J. J., Becker G. D., 2016, MNRAS, 456, 485
Stark D. P., 2016, ARA&A, 54, 761
Steidel C. C., Strom A. L., Pettini M., Rudie G. C., Reddy N. A., Trainor R. F., 2016, ApJ, 826, 159
Sugahara Y., et al., 2021, ApJ, 923, 5
Tamura Y., et al., 2019, ApJ, 874, 27
Thompson A. R., Moran J. M., Swenson George W. J., 2017, Interferometry and Synthesis in Radio Astronomy, 3rd Edition. SpringerOpen, doi:10.1007/978-3-319-44431-4
Topping M. W., Shapley A. E., Stark D. P., Endsley R., Robertson B., Greene J. E., Furlanetto S. R., Tang M., 2021, ApJ, 917, L36
Vallini L., Gallerani S., Ferrara A., Pallottini A., Yue B., 2015, ApJ, 813, 36
Vallini L., Ferrara A., Pallottini A., Carniani S., Gallerani S., 2021, MNRAS, 505, 5543
Viero M. P., Sun G., Chung D. T., Moncelsi L., Condon S. S., 2022, preprint, (`arXiv:2203.14312`)
Vijayan A. P., et al., 2022, MNRAS, 511, 4999
Vincenzo F., Matteucci F., Belfiore F., Maiolino R., 2016, MNRAS, 455, 4183
van der Walt S., Colbert S. C., Varoquaux G., 2011, Computing in Science and Engineering, 13, 22
Wang T., et al., 2019, Nature, 572, 211
Watson D., Christensen L., Knudsen K. K., Richard J., Gallazzi A., Michałowski M. J., 2015, Nature, 519, 327
Williams C. C., et al., 2019, ApJ, 884, 154
Witstok J., Smit R., Maiolino R., Curti M., Laporte N., Massey R., Richard J., Swinbank M., 2021, MNRAS, 508, 1686
Zanella A., et al., 2018, MNRAS, 481, 1976

APPENDIX A: DUST PEAK TEMPERATURE MEASUREMENTS

Here, we briefly discuss the significance of the SED peak temperature as defined in equation (9) and various measurements and predictions reported in the literature which are included in Figure 4. Importantly, the peak temperature offers a way to compare observations of the dust temperature consistently since this approach avoids degeneracies introduced by the chosen opacity model, a largely unconstrained quantity that is typically assumed to be a fixed value in the greybody spectrum (e.g. Casey et al. 2014).

For a perfect blackbody, the intrinsic temperature T_{dust} is exactly equal to the peak temperature but notably, for a greybody T_{peak} is generally lower (Casey 2012). This effect can be understood by considering a simplistic two-component dust model, where the radiation field is driven towards thermal equilibrium through absorption by the colder component in the optically thick regime, resulting in an observed outward spectrum with a peak wavelength shifted to a higher wavelength (i.e. lower T_{peak}). Vice versa, when fitting a greybody SED template, the inferred intrinsic dust temperature will strongly depend on the opacity model (e.g. Cortzen et al. 2020), while the observed peak temperature should remain the same to best fit the observed data. Indeed, T_{peak} derived from our fits is approximately unchanged under the assumption of different opacity models, while the inferred T_{dust} can change drastically: the more optically thick the SED is (i.e. the higher λ_0), the higher the resulting intrinsic temperature, T_{dust} (see Section 4.1).

In Figure 4, we show the results at lower redshifts ($0 < z < 4$) of Schreiber et al. (2018), who fit detailed SED templates built from multiple dust components to stacked spectra. Their reported dust temperatures are thus mass-weighted; however, they find a simple, linear relation where the mass-weighted temperature is roughly 91% of the luminosity-weighted one. This implies temperatures inferred from a greybody, which are necessarily weighted by luminosity, are similar to (although ~ 10% higher than) the mass-weighted temperature, effectively setting an upper limit. We also show the (partially extrapolated) linear fit obtained by Schreiber et al. (2018) and the power-law fit to the peak-temperature evolution of simulated galaxies by Liang et al. (2019).

At intermediate redshifts ($2 < z < 6$), SMGs from the SPT survey (Reuter et al. 2020) are shown as squares (all other high-redshift galaxies are circles with errorbars). In addition, results for four star-forming galaxies at $z \sim 6$ with photometric detections in three ALMA bands each are included as circles (Faisst et al. 2020). For five star-forming galaxies at $6 < z < 8$ – J1211-0118 and J0217-0208 at $z \simeq 6$ (Harikane et al. 2020), A1689-zD1 at $z \simeq 7.13$ (Knudsen et al. 2017; Inoue et al. 2020; Bakx et al. 2021), B14-65666 at $z \simeq 7.15$ (Hashimoto et al. 2019; Sugahara et al. 2021), and MACS0416-Y1 at $z \simeq 8.31$ (Tamura et al. 2019; Bakx et al. 2020) – we derive dust properties using the same MERCURIUS fit described in Section 4.1 for consistency. We allow β_{IR} to vary freely for A1689-zD1, since there are four dust continuum detections; for MACS0416-Y1, we take $\beta_{\mathrm{IR}} = 2$ as this provides a better fit. For A1689-zD1 and B14-65666 we opt for the fiducial self-consistent opacity model (we note this assumption has little impact on the inferred T_{peak}), while for MACS0416-Y1 we use an optically thin SED to obtain a conservative lower limit on the temperature (95% confidence). We also adopt an optically thin SED for J1211-0118 and J0217-0208 due to the lack of a size measurement.

APPENDIX B: SPATIALLY RESOLVED ANALYSIS

In Figure A1, we show the placements of individual regions (circles with a radius 1.5 times that of the mean circularised beam between the [C ɪɪ] and [O ɪɪɪ] observations) that were used in the spatially resolved analysis (Section 5.6). The [O ɪɪɪ] 88 µm and [C ɪɪ] 158 µm maps were created from imaging parameters that have been chosen to match beam sizes; see Table 2; the dust continuum at ∼ 160 µm has the same imaging parameters (and therefore nearly identical beam) as the [C ɪɪ] line. IR luminosities were calculated similarly as discussed in Section 4. Finally, the UV continuum has been convolved with an effective beam found by the Richardson-Lucy algorithm to match the dust continuum PSF (see also Section 5.6).

For each source, one or several regions are highlighted in the spectra and correspondingly by their number in the second row of images. From the spectra, it for instance becomes clear that, although there still seems to be some residual signal, the [O ɪɪɪ] flux is weakest in region 2 and 5 of COS-3018555981.

This paper has been typeset from a TEX/LATEX file prepared by the author.

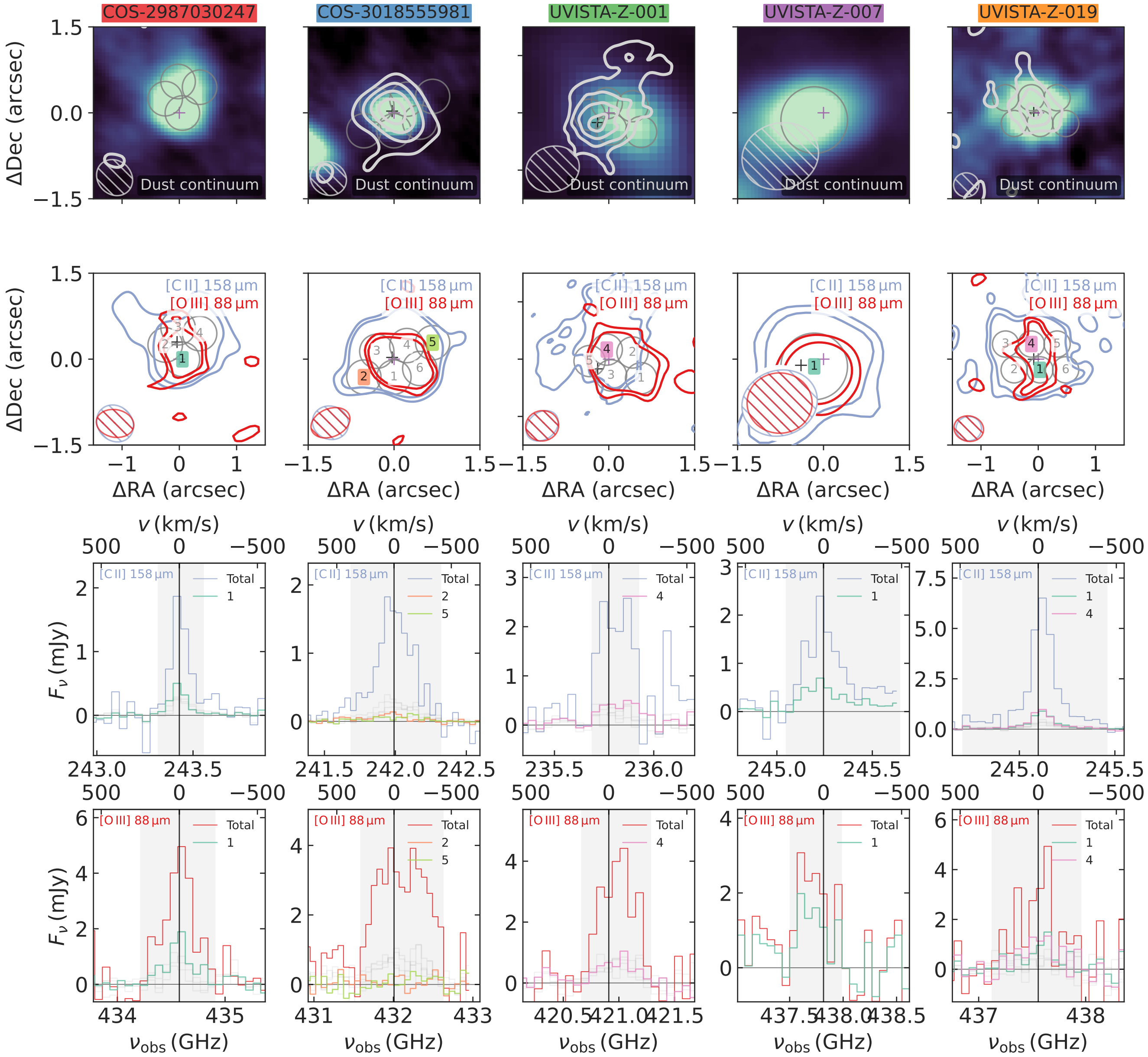

Figure A1. Beam placement for spatially resolved analysis. The top row of images shows the UV continuum with contours of the ~ 160 µm dust continuum (starting from 2σ and going up in steps of 1σ for COS-2987030247 and UVISTA-Z-019, else 2σ). The peaks of the UV and dust continua (if detected) are indicated with a black and purple cross, respectively. Contours (at 2σ and 3σ) of the [C II] 158 µm and [O III] 88 µm lines are shown in the second row (and again the UV and dust peaks). The last two rows contain their spectra, both integrated over the entire 2σ region (in the same colour as their contours) as well as for the individual regions. For each source, one or several regions are highlighted in the spectra and correspondingly by their number in the second row of images. The filled-in grey region indicates the spectral channels over which the spectra have been integrated.